



Dark Energy Survey Year 3 Results: Photometric Data Set for Cosmology

I. Sevilla-Noarbe¹, K. Bechtol², M. Carrasco Kind^{3,4}, A. Carnero Rosell^{1,5,6}, M. R. Becker⁷, A. Drlica-Wagner^{8,9,10}, R. A. Gruendl^{3,4}, E. S. Rykoff^{11,12}, E. Sheldon¹³, B. Yanny⁹, A. Alarcon^{7,14,15}, S. Allam⁹, A. Amon¹¹, A. Benoit-Lévy^{16,17,18}, G. M. Bernstein¹⁹, E. Bertin^{16,18}, D. L. Burke^{11,12}, J. Carretero^{20,21}, A. Choi²², H. T. Diehl⁹, S. Everett²³, B. Flaugher⁹, E. Gaztanaga^{14,15}, J. Gschwend^{24,25}, I. Harrison²⁶, W. G. Hartley²⁷, B. Hoyle^{28,29,30}, M. Jarvis¹⁹, M. D. Johnson⁴, R. Kessler^{8,10}, R. Kron^{9,10}, N. Kuropatkin⁹, B. Leistedt³¹, T. S. Li^{32,33}, F. Menanteau^{3,4}, E. Morganson⁴, R. L. C. Ogando²⁵, A. Palmese^{9,10}, F. Paz-Chinchón^{4,34}, A. Pieres^{24,25}, C. Pond⁴, M. Rodriguez-Monroy¹, J. Allyn Smith³⁵, K. M. Stringer³⁶, M. A. Troxel³⁷, D. L. Tucker⁹, J. de Vicente¹, W. Wester⁹, Y. Zhang⁹, T. M. C. Abbott³⁸, M. Aguena^{24,39}, J. Annis⁹, S. Avila⁴⁰, S. Bhargava⁴¹, S. L. Bridle²⁶, D. Brooks¹⁷, D. Brout^{42,65}, F. J. Castander^{14,15}, R. Cawthon², C. Chang^{8,10}, C. Conselice^{26,43}, M. Costanzi^{44,45}, M. Crocce^{14,15}, L. N. da Costa^{24,25}, M. E. S. Pereira⁴⁶, T. M. Davis⁴⁷, S. Desai⁴⁸, J. P. Dietrich²⁸, P. Doel¹⁷, K. Eckert¹⁹, A. E. Evrard^{46,49}, I. Ferrero⁵⁰, P. Fosalba^{14,15}, J. García-Bellido⁴⁰, D. W. Gerdes^{46,49}, T. Giannantonio^{34,51}, D. Gruen^{11,12,52}, G. Gutierrez⁹, S. R. Hinton⁴⁷, D. L. Hollowood²³, K. Honscheid^{22,53}, E. M. Huff⁵⁴, D. Huterer⁴⁶, D. J. James⁴², T. Jeltema²³, K. Kuehn^{55,56}, O. Lahav¹⁷, C. Lidman^{57,58}, M. Lima^{24,39}, H. Lin⁹, M. A. G. Maia^{24,25}, J. L. Marshall³⁶, P. Martini^{22,59,60}, P. Melchior³², R. Miquel^{20,61}, J. J. Mohr^{28,29}, R. Morgan², E. Neilson⁹, A. A. Plazas³², A. K. Romer⁴¹, A. Roodman^{11,12}, E. Sanchez¹, V. Scarpine⁹, M. Schubnell⁴⁶, S. Serrano^{14,15}, M. Smith⁶², E. Suchyta⁶³, G. Tarle⁴⁶, D. Thomas⁶⁴, C. To^{11,12,52}, T. N. Varga^{29,30}, R. H. Wechsler^{11,12,52}, J. Weller^{29,30}, and R. D. Wilkinson⁴¹
(DES Collaboration)

¹ Centro de Investigaciones Energéticas, Medioambientales y Tecnológicas (CIEMAT), E-28040 Madrid, Spain; ignacio.sevilla@ciemat.es

² Physics Department, 2320 Chamberlin Hall, University of Wisconsin-Madison, 1150 University Avenue, Madison, WI 53706-1390, USA; kbechtol@wisc.edu

³ Department of Astronomy, University of Illinois at Urbana-Champaign, 1002 West Green Street, Urbana, IL 61801, USA; mcarras2@illinois.edu

⁴ National Center for Supercomputing Applications, 1205 West Clark Street, Urbana, IL 61801, USA

⁵ Instituto de Astrofísica de Canarias, E-38205 La Laguna, Tenerife, Spain

⁶ Universidad de La Laguna, Dpto. Astrofísica, E-38206 La Laguna, Tenerife, Spain

⁷ HEP Division, Argonne National Laboratory, Lemont, IL 60439, USA

⁸ Department of Astronomy and Astrophysics, University of Chicago, Chicago, IL 60637, USA

⁹ Fermi National Accelerator Laboratory, P.O. Box 500, Batavia, IL 60510, USA

¹⁰ Kavli Institute for Cosmological Physics, University of Chicago, Chicago, IL 60637, USA

¹¹ Kavli Institute for Particle Astrophysics & Cosmology, P.O. Box 2450, Stanford University, Stanford, CA 94305, USA

¹² SLAC National Accelerator Laboratory, Menlo Park, CA 94025, USA

¹³ Brookhaven National Laboratory, Bldg 510, Upton, NY 11973, USA

¹⁴ Institut d'Estudis Espacials de Catalunya (IEEC), E-08034 Barcelona, Spain

¹⁵ Institute of Space Sciences (ICE, CSIC), Campus UAB, Carrer de Can Magrans, s/n, E-08193 Barcelona, Spain

¹⁶ CNRS, UMR 7095, Institut d'Astrophysique de Paris, F-75014, Paris, France

¹⁷ Department of Physics & Astronomy, University College London, Gower Street, London, WC1E 6BT, UK

¹⁸ Sorbonne Universités, UPMC Univ Paris 06, UMR 7095, Institut d'Astrophysique de Paris, F-75014, Paris, France

¹⁹ Department of Physics and Astronomy, University of Pennsylvania, Philadelphia, PA 19104, USA

²⁰ Institut de Física d'Altes Energies (IFAE), The Barcelona Institute of Science and Technology, Campus UAB, E-08193 Bellaterra (Barcelona), Spain

²¹ Port d'Informació Científica (PIC), Campus UAB, C. Albareda s/n, E-08193 Bellaterra (Barcelona), Spain

²² Center for Cosmology and Astro-Particle Physics, The Ohio State University, Columbus, OH 43210, USA

²³ Santa Cruz Institute for Particle Physics, Santa Cruz, CA 95064, USA

²⁴ Laboratório Interinstitucional de e-Astronomia—LIneA, Rua Gal. José Cristino 77, Rio de Janeiro, RJ—20921-400, Brazil

²⁵ Observatório Nacional, Rua Gal. José Cristino 77, Rio de Janeiro, RJ—20921-400, Brazil

²⁶ Jodrell Bank Center for Astrophysics, School of Physics and Astronomy, University of Manchester, Oxford Road, Manchester, M13 9PL, UK

²⁷ Département de Physique Théorique and Center for Astroparticle Physics, Université de Genève, 24 quai Ernest Ansermet, CH-1211 Geneva, Switzerland

²⁸ Faculty of Physics, Ludwig-Maximilians-Universität, Scheinerstr. 1, D-81679 Munich, Germany

²⁹ Max Planck Institute for Extraterrestrial Physics, Giessenbachstrasse, D-85748 Garching, Germany

³⁰ Universitäts-Sternwarte, Fakultät für Physik, Ludwig-Maximilians-Universität München, Scheinerstr. 1, D-81679 München, Germany

³¹ New York University, CCPP, New York, NY 10003, USA

³² Department of Astrophysical Sciences, Princeton University, Peyton Hall, Princeton, NJ 08544, USA

³³ Observatories of the Carnegie Institution for Science, 813 Santa Barbara Street, Pasadena, CA 91101, USA

³⁴ Institute of Astronomy, University of Cambridge, Madingley Road, Cambridge, CB3 0HA, UK

³⁵ Austin Peay State University, Dept. Physics, Engineering and Astronomy, P.O. Box 4608 Clarksville, TN 37044, USA

³⁶ George P. and Cynthia Woods Mitchell Institute for Fundamental Physics and Astronomy, and Department of Physics and Astronomy, Texas A&M University, College Station, TX 77843, USA

³⁷ Department of Physics, Duke University, Durham, NC 27708, USA

³⁸ Cerro Tololo Inter-American Observatory, NSF's National Optical-Infrared Astronomy Research Laboratory, Casilla 603, La Serena, Chile

³⁹ Departamento de Física Matemática, Instituto de Física, Universidade de São Paulo, CP 66318, São Paulo, SP, 05314-970, Brazil

⁴⁰ Instituto de Física Teórica UAM/CSIC, Universidad Autónoma de Madrid, E-28049 Madrid, Spain

⁴¹ Department of Physics and Astronomy, Pevenssey Building, University of Sussex, Brighton, BN1 9QH, UK

⁴² Center for Astrophysics | Harvard & Smithsonian, 60 Garden Street, Cambridge, MA 02138, USA

⁴³ University of Nottingham, School of Physics and Astronomy, Nottingham, NG7 2RD, UK

⁴⁴ INAF-Osservatorio Astronomico di Trieste, via G.B. Tiepolo 11, I-34143 Trieste, Italy

⁴⁵ Institute for Fundamental Physics of the Universe, Via Beirut 2, I-34014 Trieste, Italy

⁴⁶ Department of Physics, University of Michigan, Ann Arbor, MI 48109, USA

⁴⁷ School of Mathematics and Physics, University of Queensland, Brisbane, QLD 4072, Australia

⁴⁸ Department of Physics, IIT Hyderabad, Kandi, Telangana 502285, India
⁴⁹ Department of Astronomy, University of Michigan, Ann Arbor, MI 48109, USA
⁵⁰ Institute of Theoretical Astrophysics, University of Oslo.P.O. Box 1029 Blindern, NO-0315 Oslo, Norway
⁵¹ Kayli Institute for Cosmology, University of Cambridge, Madingley Road, Cambridge, CB3 0HA, UK
⁵² Department of Physics, Stanford University, 382 Via Pueblo Mall, Stanford, CA 94305, USA
⁵³ Department of Physics, The Ohio State University, Columbus, OH 43210, USA
⁵⁴ Jet Propulsion Laboratory, California Institute of Technology, 4800 Oak Grove Drive, Pasadena, CA 91109, USA
⁵⁵ Australian Astronomical Optics, Macquarie University, North Ryde, NSW 2113, Australia
⁵⁶ Lowell Observatory, 1400 Mars Hill Road, Flagstaff, AZ 86001, USA
⁵⁷ Centre for Gravitational Astrophysics, College of Science, The Australian National University, ACT 2601, Australia
⁵⁸ The Research School of Astronomy and Astrophysics, Australian National University, ACT 2601, Australia
⁵⁹ Department of Astronomy, The Ohio State University, Columbus, OH 43210, USA
⁶⁰ Radcliffe Institute for Advanced Study, Harvard University, Cambridge, MA 02138, USA
⁶¹ Institut^o Catalana de Recerca i Estudis Avançats, E-08010 Barcelona, Spain
⁶² School of Physics and Astronomy, University of Southampton, Southampton, SO17 1BJ, UK
⁶³ Computer Science and Mathematics Division, Oak Ridge National Laboratory, Oak Ridge, TN 37831, USA
⁶⁴ Institute of Cosmology and Gravitation, University of Portsmouth, Portsmouth, PO1 3FX, UK

Received 2021 January 4; revised 2021 February 23; accepted 2021 March 1; published 2021 May 17

Abstract

We describe the Dark Energy Survey (DES) photometric data set assembled from the first three years of science operations to support DES Year 3 cosmologic analyses, and provide usage notes aimed at the broad astrophysics community. Y3 GOLD improves on previous releases from DES, Y1 GOLD, and Data Release 1 (DES DR1), presenting an expanded and curated data set that incorporates algorithmic developments in image detrending and processing, photometric calibration, and object classification. Y3 GOLD comprises nearly 5000 deg² of *grizY* imaging in the south Galactic cap, including nearly 390 million objects, with depth reaching a signal-to-noise ratio ~ 10 for extended objects up to $i_{\text{AB}} \sim 23.0$, and top-of-the-atmosphere photometric uniformity < 3 mmag. Compared to DR1, photometric residuals with respect to Gaia are reduced by 50%, and per-object chromatic corrections are introduced. Y3 GOLD augments DES DR1 with simultaneous fits to multi-epoch photometry for more robust galactic color measurements and corresponding photometric redshift estimates. Y3 GOLD features improved morphological star–galaxy classification with efficiency $> 98\%$ and purity $> 99\%$ for galaxies with $19 < i_{\text{AB}} < 22.5$. Additionally, it includes per-object quality information, and accompanying maps of the footprint coverage, masked regions, imaging depth, survey conditions, and astrophysical foregrounds that are used to select the cosmologic analysis samples.

Unified Astronomy Thesaurus concepts: [Surveys \(1671\)](#); [Catalogs \(205\)](#); [Observational cosmology \(1146\)](#)

1. Introduction

Optical and near-infrared imaging surveys have become one of the most widely used tools to study new physics at the cosmic frontier, including dark energy, dark matter, neutrino properties, and inflation. The current generation of imaging surveys, such as Pan-STARRS1 (PS1; Chambers et al. 2016), Hyper Suprime-Cam Subaru Strategic Program (HSC-SSP; Aihara et al. 2019), Kilo-Degree Survey (KiDS; Kuijken et al. 2019), DESI Legacy Imaging Surveys (Dey et al. 2019), and the Dark Energy Survey (DES; DES Collaboration 2005, 2016) have collectively provided deep multiband imaging over nearly the entire high-Galactic-latitude sky, and cataloged more than a billion galaxies and thousands of supernovae spanning 10 billion years of cosmic history. Together with spectroscopic surveys (e.g., eBOSS Collaboration 2020; DESI Collaboration 2016), these imaging surveys yield measurements of the expansion rate and large-scale structure in the late-time universe (e.g., DES Collaboration 2018a; Hikage et al. 2019; Hildebrandt et al. 2020) that are complementary to the high-precision measurements of the early universe (Planck Collaboration 2020). Wide-area imaging surveys provide access to the largest number of galaxies for statistical analyses, and the opportunity to combine several complementary probes of the cosmic expansion history and growth of structure into the same study (e.g., DES Collaboration 2019a; Heymans et al. 2021a).

⁶⁵ NASA Einstein Fellow.

Ground-based imaging surveys of the next decade, including the Vera C. Rubin Observatory Legacy Survey of Space and Time (LSST; Ivezić et al. 2019), aim to catalog $> 10^{10}$ galaxies and $> 10^5$ Type Ia supernovae (SNe Ia) to further test the cold dark matter with a cosmological constant (Λ CDM) universe paradigm and its extensions.

The DES Collaboration has found significant benefits to developing, validating, and curating a shared reference data set to be used as the basis for most cosmological analyses (Drlica-Wagner et al. 2018). The creation of this value-added “Gold” catalog involves close collaboration between the data pipeline team and science working groups to define and validate a set of high-quality data products that are broadly useful for science analysis. We use this iterative process to prioritize algorithmic development and introduction of new data products as needed to support accurate cosmology.

The DES data set is assembled from an imaging survey using the Blanco 4 m telescope at the Cerro Tololo Inter-American Observatory (CTIO) in Chile to observe ~ 5000 deg² of the southern sky in five broadband filters, *grizY*, ranging from ~ 400 to ~ 1060 nm in wavelength, with the Dark Energy Camera (DECam; Flaugher et al. 2015). DES completed observations in January 2019, after 6 years of operations, with 10 overlapping dithered exposures at predefined positions in the sky on each filter. The primary goal of DES is to study the origin of cosmic acceleration and the nature of dark energy,

Table 1
Dark Energy Survey Data Releases

| Release | Area (sq. deg) | Depth (<i>i</i> band) | No. Objects | Photometry Uniformity (mmag) | Supplemental Data | Reference |
|-----------|-------------------|---------------------------|-------------|------------------------------------|--|---|
| SVA1 GOLD | ~250 | 23.68 | 25M | <15 | Photo-zs | https://des.ncsa.illinois.edu/sva1 |
| Y1 GOLD | 1786 | 23.29 | 137M | <15 | Photo-zs, MOF, maps | Drlica-Wagner et al. (2018) |
| DR1 | 5186 | 23.33 | 399M | <7 | None | DES Collaboration (2018b) |
| Y3 GOLD | 4946 | 23.34 | 388M | <3 | Photo-zs, SOF/MOF, maps, improved classification | This work |

Note. All releases are made public at <https://des.ncsa.illinois.edu/>. Quoted depth corresponds to signal-to-noise ratio (S/N) = 10 in 2" diameter apertures. SOF and MOF are multi-epoch pipelines described in Section 3.3.

using a variety of cosmological probes enabled by this rich data set.

Many DES Year 1 (Y1) cosmology results (DES Collaboration 2018a) used the Y1 GOLD catalog described in Drlica-Wagner et al. (2018). The emphasis of that work was to detail the data pipelines, calibration, and curation of the co-added catalog. The Y1 data set was publicly released in October 2018,⁶⁶ including the aforementioned Y1 GOLD catalog spanning an area of ~ 1800 deg 2 , together with ancillary maps of the survey properties (Leistedt et al. 2016), shear catalogs (Zuntz et al. 2018), photometric redshift catalogs (Hoyle et al. 2018), the redMaGiC (Rozo et al. 2016) catalogs used in DES Y1 results, and value-added catalogs (Sevilla-Noarbe et al. 2018; Tarsitano et al. 2018).

The co-added catalog from the first three years of data (Y3) was publicly released as DES Data Release 1 (DR1; DES Collaboration 2018b).⁶⁷ DR1 is the first DES catalog that spans the whole footprint (~ 5000 deg 2). DR1 was produced as part of an annual data processing campaign with the DES Data Management pipeline (DESDM; Morganson et al. 2018), with photometric calibration described in Burke et al. (2018).

Here, we present the core data set used in Y3 cosmologic analyses. Y3 GOLD builds upon the DR1 co-added catalog described in DES Collaboration (2018b), with additional enhancements described in Drlica-Wagner et al. (2018), and introduces several new products and algorithmic developments. A summary of previous DES data releases appears in Table 1. Key attributes of the Y3 GOLD data set are listed in Table 2.

The Y3 GOLD data set and associated documentation are a core element of DES Y3 cosmology, and are complemented and enhanced by several additional data products described in companion papers to this one, such as refined photometric redshift estimates, shear catalogs, cosmological simulations and mock DES data sets. Figure 1 shows relationships between the various DES Y3 data products. In this work, mainly devoted to Y3 GOLD, we will highlight these relationships as appropriate in the text.

In Section 2 we review DES science operations and major upgrades appearing in Y3 GOLD. We then detail the data processing for this particular release in Section 3, going into some additional detail for astrometric and photometric calibration and performance in Section 4. We characterize the depth of the survey in Section 5 and describe several value-added quantities in Section 6. Section 7 contains a description of the

maps that accompany the release. Section 8 presents usage notes for Y3 GOLD to facilitate exploration by the wider community, and we conclude in Section 9.

All magnitude quantities in this work are expressed in the AB scale unless otherwise specified.

2. The First Three Years of DES Data

In this section, we review the Wide and Supernova Survey components of DES, and detail differences between Y3 GOLD and previous releases. The data included in Y3 GOLD spans 345 distinct nights of observations with at least one observation passing quality tests from 2013 August 15 to 2016 February 12.

2.1. Survey Overview

DES used two survey modes (Neilsen et al. 2019) to meet the specific requirements of multiple cosmological probes:

1. The Wide Survey is optimized for gravitational weak lensing, galaxy clustering, and galaxy cluster cosmological probes. The Wide Survey spans ~ 5000 deg 2 imaged with 10 dithered exposures at each position in each of five broad photometric bands *grizY* (90 s exposures, except for *Y*, which employed some 45 s exposures). During the first three years of DES, most of the Wide Survey footprint was covered with four overlapping images in each band. The Wide Survey is the basis for the Y3 GOLD data set.
2. The Supernova Survey involves repeated observations of 10 DECam fields, amounting to a total of 27 deg 2 , imaged in *griz* with an approximately weekly cadence (Kessler et al. 2015; D’Andrea et al. 2018). Difference imaging analysis of the Supernovae Survey fields enables the discovery of thousands of SNe Ia, and precision photometric lightcurves are computed following Brout et al. (2019). Cosmology results based on the analysis of a subset of spectroscopically confirmed SN Ia in the redshift range of $0.2 < z < 0.85$ from the first three years of data taking, combined with other sets, have been presented in DES Collaboration (2019b). The SN exposures are co-added to produce the Y3 Deep Field data set. Deep Field processing of some of the Supernovae Survey fields, together with DECam imaging of the Cosmic Evolution Survey (COSMOS)⁶⁸ field, enables high signal-to-noise ratio (S/N) measurements of galaxies approximately 1.5–2 mag fainter than the Wide

⁶⁶ <https://des.ncsa.illinois.edu/releases/y1a1>

⁶⁷ <https://des.ncsa.illinois.edu/releases/dr1>

⁶⁸ <http://cosmos.astro.caltech.edu>

Table 2
Key Numbers and Data Quality Summary for the DES Wide Survey (Y3 GOLD; This Work) and Deep Fields (COADD_TRUTH; Reproduced from Hartley et al. 2020b)

| Parameter | Band | | | | |
|---|--------------------------------------|---|--------------------------------------|--------------------------------------|-------------------|
| | <i>g</i> | <i>r</i> | <i>i</i> | <i>z</i> | <i>Y</i> |
| Wide Survey (this work) | | | | | |
| Median PSF FWHM (arcseconds) | 1.14 | 0.98 | 0.89 | 0.85 | 0.95 |
| Median sky brightness (electrons/pixel) | 420 | 1113 | 3386 | 7600 | 2807 ^a |
| Median sky brightness uncertainty (mag/arcsec ²) | 26.0 | 25.6 | 25.0 | 24.3 | 23.1 |
| Sky coverage (<i>grizY</i> intersection, deg ²) | | | 4946 | | |
| Co-add astrometric precision (total distance, mas) | | 28 (internal); 158 (versus Gaia DR2) | | | |
| SOF photometric uniformity versus Gaia (mmag) ^b | | 2.2 | ... | ... | ... |
| Median co-add magnitude limit, 2" diameter (S/N = 10) | 24.3 | 24.0 | 23.3 | 22.6 | 21.4 |
| Co-add 90% completeness limit for extended objects (mag) | 23.4 | 23.0 | 22.6 | 22.2 | ... |
| Multi-epoch galaxy magnitude limit (S/N = 10, SOF) ^c | 23.8 _{-0.3} ^{+0.2} | 23.6 _{-0.3} ^{+0.2} | 23.0 _{-0.2} ^{+0.2} | 22.4 _{-0.2} ^{+0.2} | ... |
| Co-add galaxy selection (EXTENDED_CLASS_MASH_SOF ≥ 2 , MAG_SOFR_I ≤ 22.5) | | Efficiency $> 98.5\%$; Contamination $< 1\%$ | | | |
| Co-add stellar selection (EXTENDED_CLASS_MASH_SOF ≤ 1 , MAG_SOFR_I ≤ 22.5) | | Efficiency $> 95\%$; Contamination $< 8\%$ | | | |
| Object density (arcmin ⁻²) ^d | | Overall: 15.5; Galaxies: 10.5 | | | |
| Deep Fields (Hartley et al. 2020b) | | | | | |
| Median PSF FWHM (arcseconds) | 1.2 | 0.96 | 0.86 | 0.73 | 1.22 ^e |
| Median co-add magnitude limit, 2" diameter, S/N = 10) | 26.0 | 25.6 | 25.0 | 24.3 | 22.5 ^e |
| Sky coverage (<i>ugrizJHKs</i> intersection, deg ²) | | | 5.88 | | |

Notes. For parameters representing a distribution, the median or mean values are quoted as specified in the main text. All magnitudes are in the AB system.

^a *Y*-band exposures are half the exposure time of the other bands; only after Y4 were 90 s exposures taken.

^b Photometric uniformity measured versus Gaia's *G* band, which encompasses DECam's *gri*; see footnote in Section 4.4.

^c Median values with 16% and 84% percentile errors from the magnitude limit distribution.

^d Object density determined for all objects in the Y3 GOLD footprint outside foreground and bad regions, and the subset of those classified as high-confidence galaxies (EXTENDED_CLASS_MASH_SOF = 3).

^e Not every deep field has *Y*-band measurements; see Hartley et al. (2020b) for details.

Survey (Hartley et al. 2020a). A subset of these data have been combined with deep near-infrared imaging to produce a reference object catalog used for various applications in DES Y3 cosmologic analyses. The Supernovae Survey data and the Y3 Deep Field data are not part of the Y3 GOLD data release.

Exposures were acquired during the allocated nights for DES at the Blanco Telescope and transferred to the National Center for Supercomputing Applications (Honscheid et al. 2012) for further processing (Section 3). A total of 38850 exposures were acquired, across all bands, and included in the Y3 Wide Survey processing (Morganson et al. 2018). The supernova cosmology program used 6877 exposures (D'Andrea et al. 2018) from the Y3 period.

The DES footprint, including the Wide and Supernovae Surveys, as well as relevant external data sets mentioned in this paper, are shown in Figure 2.

2.2. Y3 GOLD Data Set and Differences Relative to Previous DES Releases

Below, we summarize commonalities and differences in input data, image processing, and catalog generation between Y3 GOLD and previous releases. Figure 3 shows the progression in areal coverage and depth from the Science Verification phase through the completed six seasons of DES.

2.2.1. Differences Relative to Y1 GOLD

1. The Wide Survey area has increased by a factor of 2.7, from 1786 deg² to 4946 deg² with simultaneous coverage in *griz*. The exact choice of survey property selections for

specific science analyses can modify the final footprint size.

2. Co-add depth has slightly increased with respect to Y1 GOLD. Y3 focused on expanding the area and uniformity of the Y1 data set, and thus the increase in depth was fairly small.
3. The Y3 astrometric calibration is performed exclusively based on Two Micron All Sky Survey (2MASS; Skrutskie et al. 2006) instead of the Fourth US Naval Observatory CCD Astrograph Catalog (UCAC-4; Zacharias et al. 2013) used in Y1 GOLD, for the first single-epoch pass. Gaia (Gaia Collaboration 2016; Brown et al. 2018) catalogs were not available during development of the Y3 co-add processing; however, these catalogs will be used in future DES data processing campaigns (Section 4.1).
4. The Y3 photometric calibration adopts the forward global calibration method (FGCM; Burke et al. 2018) as the default algorithm for this purpose, as described in DES Collaboration (2018b; also see Section 4.3).
5. Improved pipelines have led to some changes in the flagging of objects. This is especially true with the introduction of the IMAFLAGS_ISO flag. This is a SExtractor output that provides an “OR” of all flags set in the image over all pixels in the objects' isophote, which enables the identification of image artifacts and affected objects.

2.2.2. Differences Relative to DR1

1. In Y3 GOLD, the morphological and photometric measurements are based on the Multi-Object Fitting pipeline

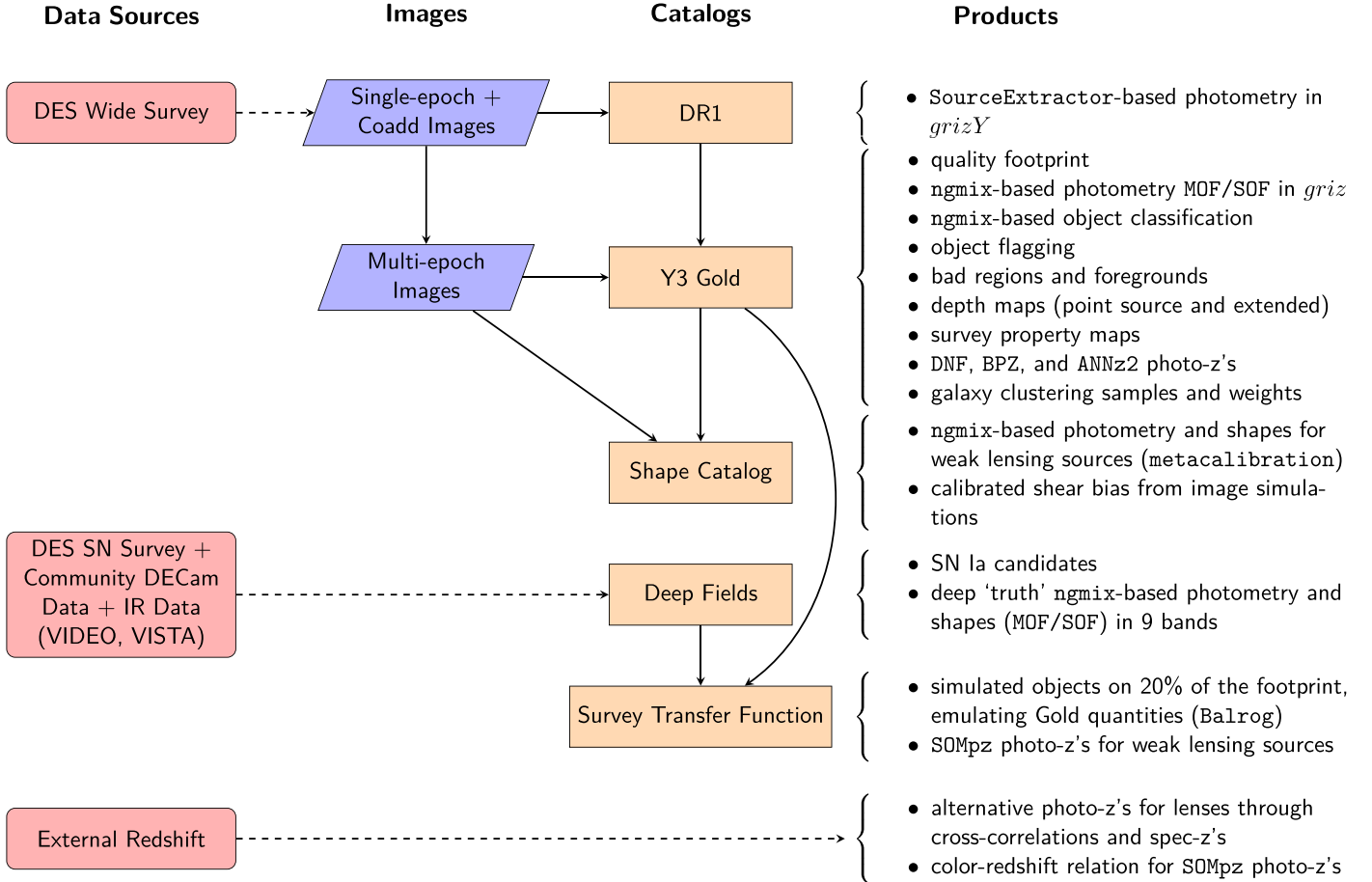


Figure 1. The Y3 DES core data sets and their relationships. Arrows indicate information flow from data sources (observations, dashed lines) or processed images and catalogs (continuous lines) to another catalog or data product. The “Products” column indicates the outputs associated with the catalogs immediately to their left.

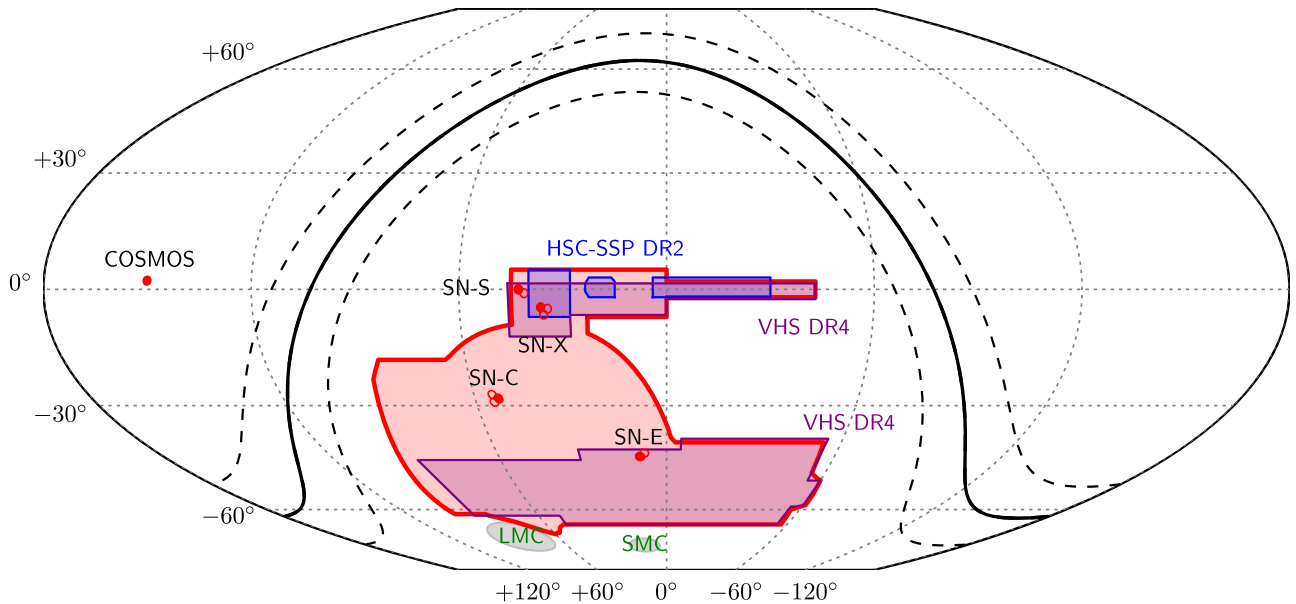


Figure 2. The DES footprint in equatorial coordinates, including the Wide Survey, the Supernova Survey fields (labeled “SN”; D’Andrea et al. 2018), the COSMOS field, as well as relevant HSC-SSP DR2 (Aihara et al. 2019) and VHS DR4 (McMahon et al. 2013) data sets used in this work (only the approximate overlapping regions are indicated for clarity). The fields used for DES Deep Field processing are filled red (Section 3.4). The DES footprint avoids the Galactic plane (solid black line with dashed lines at $b = \pm 10^\circ$) and central regions of the Large and Small Magellanic Clouds (LMC, SMC).

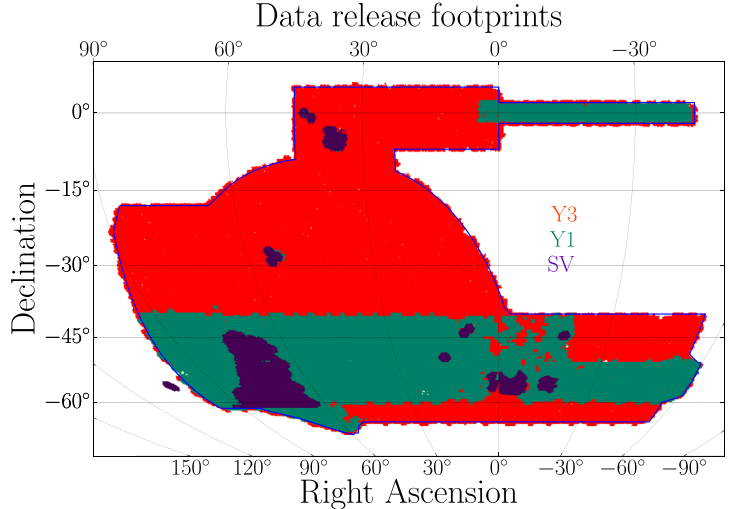
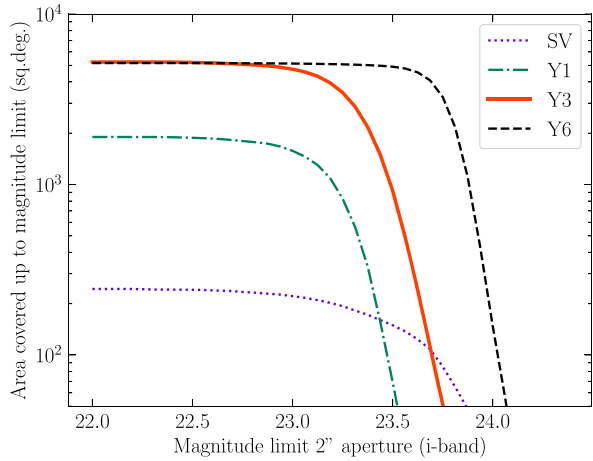


Figure 3. Left: area covered to a certain magnitude limit in 2'' diameter apertures for each data release in the i band. Right: survey map for the Science Verification (SV) Year 1 (Y1) and Year 3 (Y3) data sets (which overlap mostly the previous ones). Year 6 data covers a very similar footprint as Y3 to a greater depth.

(MOF; Drlica-Wagner et al. 2018) and its variant, the Single-Object Fitting pipeline (SOF; Section 3.3).

2. In Y3 GOLD, zero-point estimates incorporate Year 4 imaging (which was already available as single-epoch images at the time of creation of the co-added Y3 catalogs; see Appendix A.3 for details). This was due to poor sky conditions during Year 3 Y3 GOLD adds chromatic and SED-dependent interstellar extinction corrections based on a spectral template for each individual co-add object (Section 4.3).
3. Y3 GOLD includes an updated set of flags relative to Y1 GOLD to indicate various measurement anomalies (Section 6.2).
4. Y3 GOLD includes updated photometric redshifts produced with the BPZ (Benítez 2000), DNF (De Vicente et al. 2016), and ANNz2 (Sadeh et al. 2016) algorithms (Section 6.3).
5. The catalog includes a flag to indicate whether a given object lies within the Y3 GOLD footprint used for Y3 cosmologic analyses, instead of making any kind of fixed selection over the extracted sources. Accordingly, all objects from Y3 processing are included in Y3 GOLD. This approach allows alternative footprint definitions needed for specific science cases (Section 7.1).
6. The survey masks are now separated into astrophysical foregrounds (e.g., bright stars and large nearby galaxies) and “bad” regions with recognized data processing issues (Section 7.2).
7. Y3 GOLD includes maps of survey properties, such as airmass, seeing, and sky brightness, generated from combinations of image-level measurements (Section 7.3 and Appendix E).

2.2.3. Differences Relative to Y1 GOLD and DR1

1. Y3 GOLD star–galaxy separation is performed using MOF and SOF quantities, as recommended in Sevilla-Noarbe et al. (2018; see Section 6.1 and Appendix B).

3. Data Processing

The DESDM framework processes raw data acquired by DECam and produces the calibrated images and catalogs used for science. In this section, we review the overall system, and refer readers to Morganson et al. (2018) for a detailed description of the pipeline used for Y3 GOLD.

3.1. Single- and Multi-epoch Image Processing

Individual DECam exposures must be detrended for diverse instrumental signatures. This single-epoch processing stage produces calibrated images and catalogs, which are made available periodically at the National Science Foundation’s (NSF’s) National Optical-Infrared Astronomy Research Laboratory archive.⁶⁹ The single-epoch calibrated images are the basis of the shape catalogs (Gatti et al. 2021), and are referenced later by the pipeline to fit the multi-epoch photometry for the MOF, SOF, and METACALIBRATION codes (see Section 3.3).

The Y3 GOLD data set is based on the imaging products from a subsequent co-addition, which has a fainter object detection limit due to the combination of the single-epoch images. At the same time, the weight maps that are produced during the single-epoch processing are used to build depth maps using the mangle (Swanson et al. 2008) software.

3.2. Catalog Generation

Base object detections are obtained using SExtractor with the settings described in Morganson et al. (2018), tuned for an efficient extraction of $S/N \sim 10$ objects from the $r + i + z$ co-add (or detection) images. For these objects, we measure various quantities with several pipelines. The base catalog for Y3 GOLD is identical to the DR1 catalog, i.e., approximately 399 million objects. However, the definition of the Y3 GOLD footprint in Section 7.1 removes ~ 11 million objects that lie in areas where *griz* coverage criteria are not met. Multi-epoch image “postage stamps” (i.e., MEDS files; Jarvis et al. 2016) are created at this stage for each source, and used for a variety

⁶⁹ <https://astroarchive.noao.edu/>

of purposes, including the multi-epoch fitting pipelines (Section 3.3).

3.3. Single- and Multi-object Fitting Pipeline on Multi-epoch Data

Drlica-Wagner et al. (2018) described the advantages of performing a multi-object, multi-epoch, multiband fit (MOF) to the object shape to determine the morphology and flux, and we refer the reader to that paper for details of this process, based on the `ngmix` software (Sheldon 2014). In Y3 GOLD, we introduce a variant, called SOF, that simplifies the fitting process by eliminating the multi-object light-subtraction step, speeding up the processing time by a factor of a few, with a negligible impact in performance (as shown in Section 6.3). In addition, SOF has fewer objects with fit failures.

Both MOF and SOF employ `ngmix` to fit objects using reconstructed point-spread functions (PSFs) modeled as mixtures of three Gaussians at the coordinates in the MEDS files where an object was detected in the co-adds. For each object, there are as many of these stamps as there are epochs and bands observed at those coordinates. The fitting is performed for several objects simultaneously, identified with a friends-of-friends algorithm. In a first step, a bulge-plus-disk model is fit to each object in the group separately (masking the pixels containing other objects). In this way, we obtain the SOF quantities. In subsequent iterations, we can subtract the flux from these Gaussian mixture models obtained from the neighbors for each particular source (MOF). `ngmix`-based photometry generally provides a tighter reconstruction with respect to SExtractor quantities.

DES Y3 cosmology uses METACALIBRATION photometry (Huff & Mandelbaum 2017; Sheldon & Huff 2017; Zuntz et al. 2018) for source galaxies in weak-lensing analyses, as described in Gatti et al. (2021). Similarly to the MOF and SOF pipelines, the METACALIBRATION photometry is measured from all epochs and bands, but using a simplified Gaussian model for the PSF, and with an artificial shear applied to the images to obtain four different versions of the photometry. A fifth set of measurements corresponds to the unsheared version (see Zuntz et al. 2018 for more details).

Photometric redshifts are generated from the SOF photometry within the DESDM pipeline, using the Bayesian photometric redshift code, BPZ (Benítez 2000) that provides several point estimates and uncertainty estimates. The fluxes and magnitudes computed from the SExtractor- and `ngmix`-based pipelines are also the basis for other photometric redshift estimates, including those from the DNF (De Vicente et al. 2016), ANNz2 (Sadeh et al. 2016), and SOMpz (Myles et al. 2020) algorithms, which are used for various purposes in DES Y3 cosmology (see Section 6.3).

3.4. Deep Field Data Set Creation

As mentioned in Section 2.1, the SN Survey repeatedly observed 10 fields to identify transient phenomena that can later be ascribed to SNe Ia (Kessler et al. 2015). Taking advantage of these data and in parallel to the Y3 GOLD data set, Hartley et al. (2020b) have constructed the Deep Field data set to complement and enhance the main survey in the Y3 cosmologic analyses. Up to 90 images of the same patches of the sky have been stacked to achieve a depth of $gri z = [26.03, 25.63, 25.06, 24.31]$, respectively, for $S/N = 10$ in $2''$ diameter

apertures. A modified pipeline with new software to handle the higher source density and addition of near-infrared images has resulted in an eight-band catalog (*ugrizJHKs*) of 1.7 M objects over a total area of 5.88 deg^2 , after artifact masking. The Deep Field processing and data products are fully described in Hartley et al. (2020a). One of its applications is the creation of the Balrog simulations (Everett et al. 2020), in which Deep Field sources are injected into the Wide Survey images in order to understand the DES transfer function, among other uses such as for checks of the Y3 GOLD catalog (see Section 5).

4. Astrometric and Photometric Calibration

We describe here the astrometric and photometric calibration performance of the Y3 GOLD catalog. Details of the pixel-level instrument response model and associated astrometric and photometric calibrations are presented in Bernstein et al. (2017a) and Bernstein et al. (2017b). Description of the relative photometric calibration pipeline can be found in Burke et al. (2018).

4.1. Astrometric Solution

The DES Y3 astrometric solution was found via the SCAMP software using 2MASS (Skrutskie et al. 2006) stars, as described in Morganson et al. (2018). As a first pass, an initial solution is found per exposure. During co-addition, overlapping images of the same reference objects can be used to refine the solution, simultaneously using the whole catalog of objects from multiple exposures falling within that “tile” (DESDM’s sky unit for co-add processing; $0^\circ.73 \times 0^\circ.73$).

4.2. Astrometric Performance

We present updated absolute astrometric accuracy measurements for the co-add catalog (DES Collaboration 2018b) relative to the Gaia DR2 catalog (Brown et al. 2018) as an external reference. A $0''.5$ matching radius is used against all Gaia’s raw sources.⁷⁰ The result of the comparison is shown in Figure 4. This analysis shows a median of 158 mas between Y3 GOLD and Gaia DR2 positions, with a median of 28 mas between re-observations by DES.

A systematic trend, already noted in DES Collaboration (2018b), is visible in the astrometric residuals across the survey footprint. This is at least in part due to the unaccounted for proper motion effect from the 2MASS star catalog used as a reference in the solution. Celestial coordinate corrections can be obtained by fitting two 2D polynomials to the residual distribution in each coordinate, which are not included in the Y3 GOLD catalog celestial position columns but will be made available upon public release of the Y3 GOLD data set as separate coordinates for each object. This subarcsecond precision correction is estimated to be negligible for Y3 cosmology results. More recent DES processing uses the Gaia DR2 catalog as a reference (see Bernardinelli et al. 2020 for an example using Gaia DR1). Upon release of the Y3 GOLD data set, solutions from the `WCSFit` software (Bernstein et al. 2017a) for subarcsecond corrections to astrometry will be made available.

⁷⁰ <http://cdn.gea.esac.esa.int/Gaia/gdr2/>

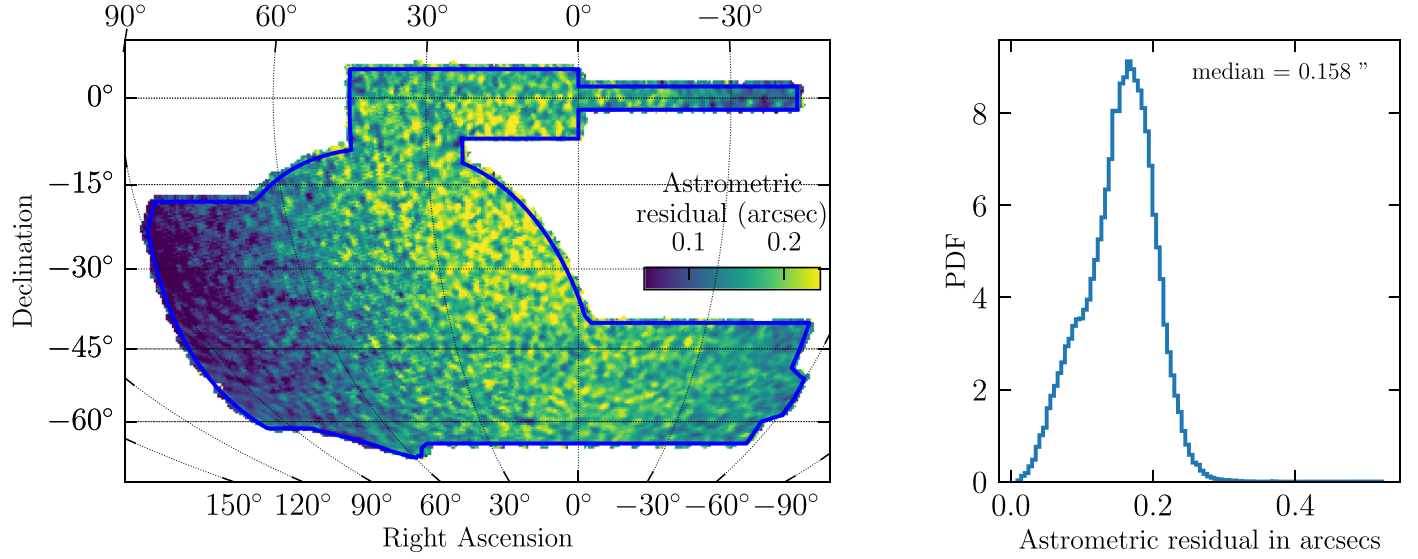


Figure 4. Astrometric residuals of Y3 GOLD vs. Gaia’s DR2 objects, computed as the median value of the modulus of the displacement vectors between the matched stars of both catalogs.

4.3. Photometric Calibration and Corrections

The Y3 GOLD photometric calibration is based on FGCM introduced by Burke et al. (2018). FGCM calibrates the entire survey using a forward modeling approach that incorporates atmospheric and instrumental behavior, obtaining the best-fit parameters of such a model, rather than performing a global minimization of the fluxes from detected stars with respect to a network of secondary standards (the latter was done in Y1 GOLD; see Drlica-Wagner et al. 2018).

Our objective is to report top-of-the-Galaxy⁷¹ energy fluxes in *griz* (AB magnitudes) corresponding to the particular spectral energy distribution (SED) of each individual co-add object as observed through the DES Y3A2 standard passband (DES Collaboration 2018b) with a precision of several millimagnitudes (Y3A2 being the internal release version). We aim to account for all photometric calibration effects possible and study their impact on photometric redshifts, and test the FGCM methodology for future applications that require millimagnitude precision (e.g., The LSST Dark Energy Science Collaboration 2018). To achieve a sub-percent photometric calibration, we include chromatic corrections that account for differences in the system response that arise from observing objects with different SEDs through passbands that vary with environmental conditions and instrument coordinates (Li et al. 2016). Our implementation in Y3 GOLD includes three steps: (1) zero-points computed from FGCM fits for each and every CCD image for use in image co-addition and transient analyses, (2) chromatic corrections corresponding to per-object SED templates, and (3) interstellar extinction corrections that optionally include the per-object SED dependence. We briefly describe the fiducial calibration steps here and provide the detailed formalism in Appendix A.

⁷¹ “Top-of-the-Galaxy” refers to the source spectrum incident at the Milky Way before reddening by interstellar dust. “Top-of-the-atmosphere” refers to the source spectrum incident at the top of the Earth’s atmosphere after reddening by interstellar dust. The majority of faint halo stars detected by DES are expected to be located beyond most of the total dust column (Jurić et al. 2008), and thus correcting the inferred top-of-the-atmosphere spectra assuming the full dust column provides a good approximation of their intrinsic spectra.

Prior to co-addition, each CCD image was assigned an FGCM zero-point assuming that the bright stars used as calibration sources share the SED of a spectrophotometric standard, specifically the G star C26202 (Bohlin et al. 2014). For Y3 GOLD, we update the zero-points incorporating Year 4 imaging for the purpose of calibration only. This was necessary due to bad sky conditions throughout the third year preventing adequate uniformity in the calibration, and faulty global positioning system (GPS) data that spoiled the FGCM solutions. We additionally made improvements to aperture corrections, updates to the DES Y3A2 standard bandpass, and other technical modifications to the FGCM procedure (E. S. Rykoff et al. 2021, in preparation). This correction corresponds to the `DELTA_MAG_Y4` quantities. These updates are possible without a complete co-addition thanks to the scheme described in Appendix A.

Next, we associate a spectral template with each individual co-add object based on the preliminary co-add photometry. We use the Pickles (1998) stellar spectral library for high-confidence stars, and the COSMOS SED library (Ilbert et al. 2009) for galaxies and ambiguous objects. We fit SED templates together with preliminary photo-*z* estimates. Using these spectral templates, we compute per-object chromatic corrections to obtain top-of-the-atmosphere calibrated fluxes as observed through the DES Y3A2 standard bandpass. This correction corresponds to the `DELTA_MAG_CHROM` quantities.

Finally, we calculate per-object SED-dependent interstellar extinction corrections using the same SED templates for several dust reddening maps, including those of Schlegel et al. (1998), Planck Collaboration (2014), and Lenz et al. (2017). Additional details are provided in Appendix A.5. This correction corresponds to the `A_SED` quantities.

While we have focused on chromatic corrections for precision photometry, we note that per-object SED templates could be used for other data processing steps that are sensitive to chromatic effects, such as PSF modeling and differential chromatic refraction (Meyers & Burchat 2015; Erikson & Hoekstra 2018; Carlsten et al. 2018). The general procedure developed here may be applicable to other imaging surveys with increasingly stringent systematic error budgets, such as

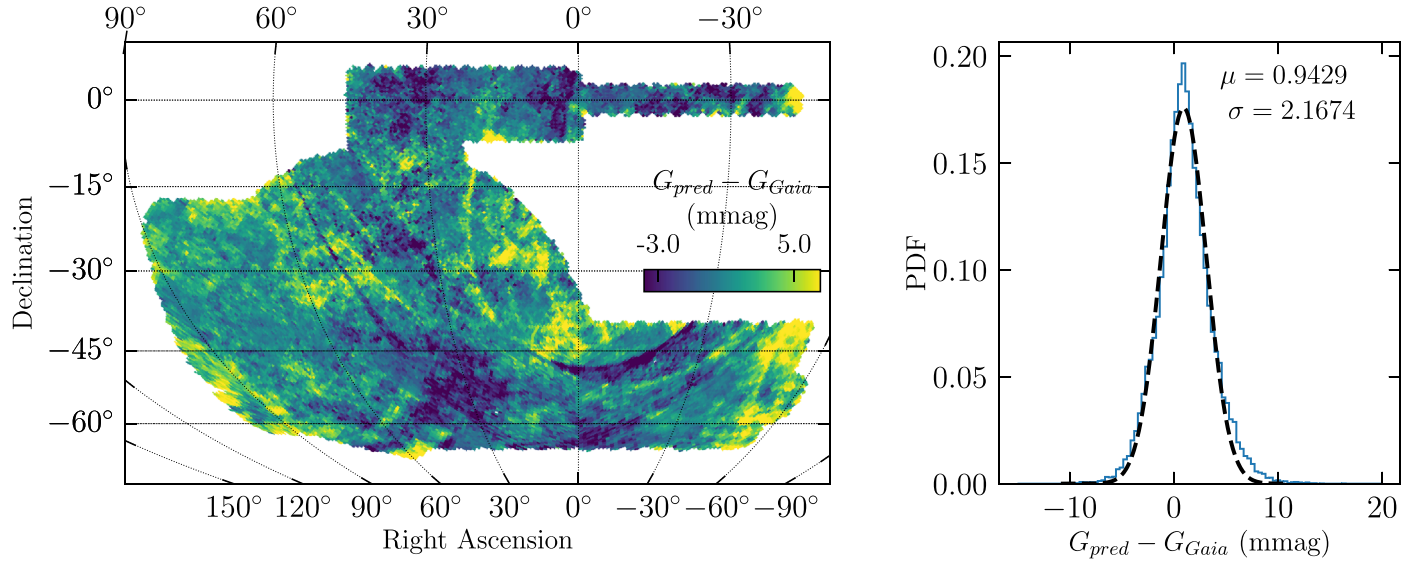


Figure 5. Photometric residuals of DES stars vs. Gaia DR2 counterparts, transforming DES fluxes to Gaia’s G band (see footnote in Section 4.4). Some of the arc-like spatially correlated residual features match the Gaia scanning pattern.

those of the Rubin Observatory and Euclid (e.g., Galametz et al. 2017).

4.4. Photometric Performance

Summary statistics for the relative photometric calibration of Y3 GOLD are reported in Table 2. We refer the reader to DES Collaboration (2018b) for detailed information on the calibration of DES photometry to a physical (AB magnitude) scale, which was assessed via repeated observations of a CALSPEC standard star, C26202 (Bohlin et al. 2014).

Figure 5 shows updated results for the top-of-the-atmosphere photometric uniformity measured against Gaia DR2. Relative to DES Collaboration (2018b), use of Y4 zero-points, improvements in the FGCM pipeline, and application of chromatic corrections have decreased the scatter of photometric residuals versus Gaia photometry (transformed to Gaia’s G band⁷²) from ~ 7 mmag to < 3 mmag. Importantly, DES and Gaia photometric calibration pipelines are completely independent from each other, implying that at least one of these surveys has photometric uniformity of better than ~ 1.4 mmag.

The top-of-the-atmosphere calibration in Y3 GOLD has reached a level of precision such that the treatment of interstellar extinction is now a limiting source of systematic uncertainty affecting the photometry of most DES objects. Differences between varying prescriptions for interstellar extinction corrections are typically $\gtrsim 10$ mmag for object colors, even in the low-extinction regime that characterizes the DES footprint (see Appendix A.5 for details). Whereas inclusion of additional overlapping exposures in the co-add tends to improve uniformity and average down differences between the observed passband and the standard bandpass, such that chromatic corrections are reduced, uncertainty in both the normalization of the dust opacity as well as chromatic effects of interstellar extinction persist.

⁷² This transformation is performed using a subset of common stars between Gaia and DES FGCM standards as a training set for a random forest, which is built to transform stellar photometry from one system to the other. This transformation uses DES gri magnitudes and colors as features in the training, and is valid for the interval $0.5 < g - i < 1.5$.

When comparing the primary photometric methods for point-like (SOF_PSF_MAG_I) and extended objects (SOF_CM_MAG_I) for high-confidence stars, we find an average systematic offset in each of the $griz$ bands that varies at the level 0.02 mag between bands. The SOF_PSF_MAG_I agrees well with the SExtractor PSF photometry used by FGCM for photometric calibration of the survey in all of the $griz$ bands. Accordingly, there might be a systematic color offset for galaxies at the 0.02 mag level. We do not expect this color offset to substantially affect photometric redshift methods that are trained and evaluated consistently; however, template-fitting methods might be impacted. Several dedicated studies have been performed to validate the photo-z distribution of samples used for DES Y3 cosmology.

5. Depth

The depth of Y3 GOLD can be quantified using several approaches, as detailed in DES Collaboration (2018b). Here, we focus on the effective depth obtained using the SOF photometry, which is unique to Y3 GOLD, and on measurements of the detection completeness of the galactic population.

5.1. Depth from SOF Photometry for Galactic Analyses

In order to have a more accurate description of $S/N = 10$ depth for galactic photometry (using the SOF model magnitudes), we follow the procedure described in Rykoff et al. (2015) in which a model is trained on a coarse $n_{\text{side}} = 1024$ HEALPix pixelization using several survey properties as features. The depth within the coarse pixels is estimated by fitting the magnitude versus magnitude error function. This fit is done only for extended objects with $\text{EXTENDED_CLASS_MASH_SOF} > 1$ (with a median ~ 1.9 pixel semimajor axis length) to capture the depth for galaxy-like sources. The model is then applied to pixels in default survey property map resolution ($n_{\text{side}} = 4096$) to produce the reference depth map for that photometry.

This results in the following estimates, again taking the median of the histogram distribution: $griz = [23.8, 23.6, 23.0,$

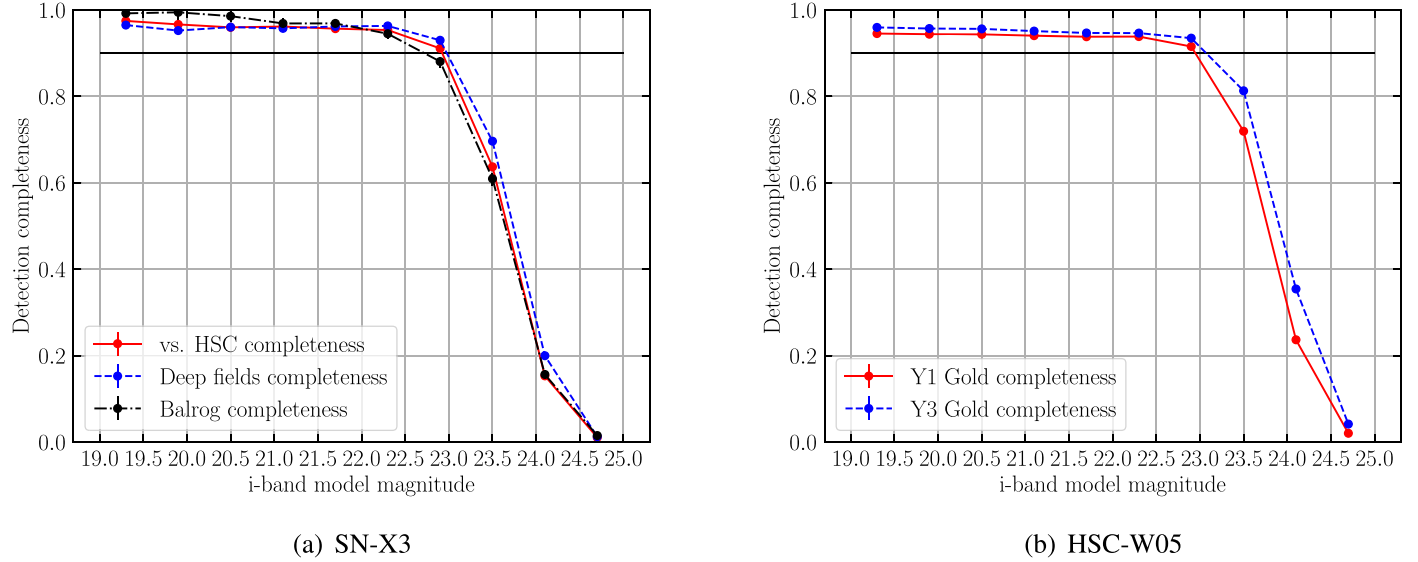


Figure 6. Left: detection completeness for extended objects in the SN-X3 field ($\alpha, \delta \sim 362^\circ, -4^\circ$; approximately 3 deg^2 in area) in the i band, comparing three methodologies: using a deeper external data set (HSC-SSP DR2, ~ 360 thousand matches to Y3 GOLD), the Deep Field catalog in that region, and simulations from Balrog processing, which inject realistic images onto co-added Y3 images. Similar agreement is obtained in other bands. Right: detection completeness for extended objects in the HSC-SSP W05 field ($\alpha \sim 330^\circ\text{--}360^\circ, \delta \sim 0^\circ$; approximately 90 deg^2 in area of overlap) in the i band, comparing Y1 GOLD and Y3 GOLD vs. the Wide Field HSC-SSP DR2 data set (~ 4.9 million matches to Y3 GOLD). Note that this region is wider and more representative of Y3 GOLD than the comparison shown in Figure 6(a) and is 0.23 magnitudes deeper. Errors are 95% containment errors computed using a Bayesian approach for efficiencies as detailed in Paterno (2004) but cannot be visualized as they are small compared to the data markers themselves. The black solid horizontal line represents the 90% level for visual reference.

22.4]. These values are a more accurate representation of the galactic photometry since a selection of galaxies with good properties is used to obtain the magnitude limit estimates. These depth estimates include chromatic corrections and the extinction model described in Section 4.3. For comparison, the MOF $S/N = 10$ depth from Y1 GOLD in $griz = [23.7, 23.5, 22.9, 22.2]$.

5.2. Detection Completeness

An alternative to the signal-to-noise threshold depth measurement is characterization of the object detection completeness as a function of magnitude. We use the HSC-SSP Data Release 2 (DR2; Aihara et al. 2019), which reaches a depth of $i \sim 26.2$ for point sources at $S/N = 5$, for the Wide Survey, significantly deeper than the DES Year 3 data set. For Y3 GOLD data, we have at our disposal additional techniques that can be used as crosschecks, namely deeper observations with DECam through Deep Fields processing (Hartley et al. 2020b) and the Balrog simulations (Everett et al. 2020).

We use as a common mask for both data sets the Y3 GOLD footprint and foregrounds mask, defined in Section 7.2 coupled with the HSC star masks from the latest iteration (S18A⁷³). Similarly, we combine the Y3 GOLD masks with the Deep Field data sets, which incorporates its own set of masks. We perform a $0.5''$ matching between each catalog and Y3 GOLD in this region with these constraints. The Balrog data set contains its own self-matching with similar characteristics, and the catalog already includes objects that have been detected with a flag.

Results (for extended objects) are shown in Figure 6(a), where we see good agreement between the various methodologies, and Figure 6(b) where a comparison with Y1 GOLD completeness is shown. We note that the completeness

presented here is different from that computed in Kessler et al. (2019): completeness for the SN Ia cosmologic analysis was computed as a function of supernova peak i -band magnitude rather than as a function of its host galactic magnitude (Figure 4 of Kessler et al. 2019).

5.3. Stellar Obscuration

Ross et al. (2011) noted the effect of obscuration around point sources as a systematic effect for clustering, and quantified the impact through measurements of the under-density of galaxies around these sources. A similar measurement for DES has been done around VVDS sources and is shown in Figure 7, and for a region closer to the Galactic plane in Figure 7(b). The obscuring radius is slightly larger in the case of the field near the plane, which will impact the galactic distribution, and is addressed using correction weighting, as developed in M. Rodríguez-Monroy et al. (2021, in preparation) and Elvin-Poole et al. (2018). Alternatively, or in addition to this approach, a mask can be built around stellar objects (`EXTENDED_CLASS_MASH_SOF = 0, $i < 20$`) with a $5''$ radius to remove them together with the exclusion radius found here.

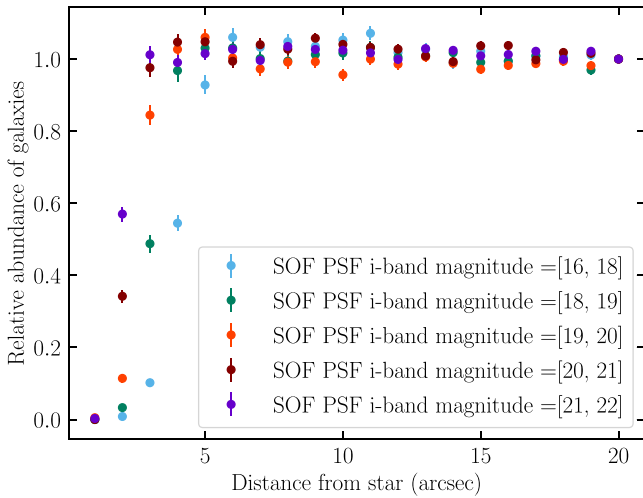
6. Object Characterization

In this section, we report on several additional flags and labels computed for each object in the catalog.

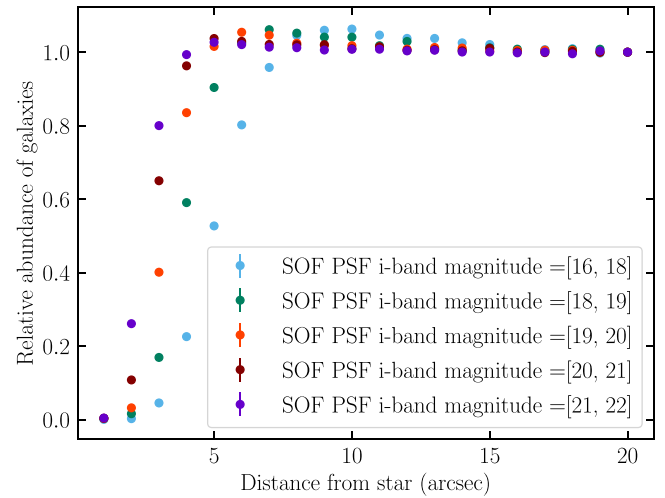
6.1. Object Classification

The MOF and SOF pipelines provide a better measurement of the extension of a given object, as compared with co-add quantities, as shown in Sevilla-Noarbe et al. (2018), where insufficient modeling of PSF variations and discontinuities can have an important impact in the selection of objects with similar characteristics even when close to each other.

⁷³ <https://hsc-release.mtk.nao.ac.jp/doc/index.php/bright-star-masks-2/>



(a) SN-X3



(b) Near Galactic plane

Figure 7. Left: stellar obscuration in the SN-X3 field as a function of distance from the star, expressed as the deficit of galactic density with respect to the density of galaxies at $20''$, binned within several intervals of `SOF_PSF_MAG_I`. Right: same in a region at $b = [-38, -31]$ degrees, closer to the Galactic plane. The obscuration effect is slightly larger in radius, due to overlap with other obscuring stars.

For Y3 GOLD, we have created a set of EXTENDED_CLASS classifiers that group objects according to their consistency with a point-like morphology, with a higher value corresponding to more spatially extended shapes (details in Appendix B). Here we summarize the performance, including completeness and purity characterization for stars and galaxies, for our default classifier `EXTENDED_CLASS_MASH_SOF`.

We can validate the bright end of the classification using additional infrared data from the VISTA Hemisphere Survey (VHS; McMahon et al. 2013) as demonstrated in Baldry et al. (2010) and Sevilla-Noarbe et al. (2018). We perform a $0''5$ astrometric match to overlapping VHS sources, and define a stellar versus nonstellar classification based on $g - i$ DES optical color versus $J - Ks$ VHS color. The result of such separation in this space is seen in Figure 8.

Using this clean color-based classification scheme as a “truth” reference, it is possible to evaluate the quality of the EXTENDED_CLASS_MASH_SOF classification at the bright end of the magnitude distribution (approximately from 15 to 21 in the i band, where a significant number of matched VHS objects are available). From this comparison, we can deduce two useful performance indicators for galactic samples that are relevant for cosmologic analyses: purity (also called precision or positive predictive value) or equivalently, contamination as $(1 - \text{purity})$, and efficiency (also called completeness, or true-positive rate). Figure 9(a) shows these results for a match to the VHS catalog over the overlapping footprint. Near the saturation threshold of DES, we see that up to $\sim 30\%$ of objects classified as morphologically extended have colors that are more consistent with being stars. Some fraction of these objects might be double stars, and should be eliminated from galactic samples. The galactic samples used for DES Y3 cosmology do not include this population of bright objects due to flux and/or color selections.

We can also use deeper surveys with good seeing and/or space-based imaging to provide a morphological reference to validate the star–galaxy classifier for fainter objects. We used the W02 field of the HSC-SSP DR2 catalog (Aihara et al. 2018),

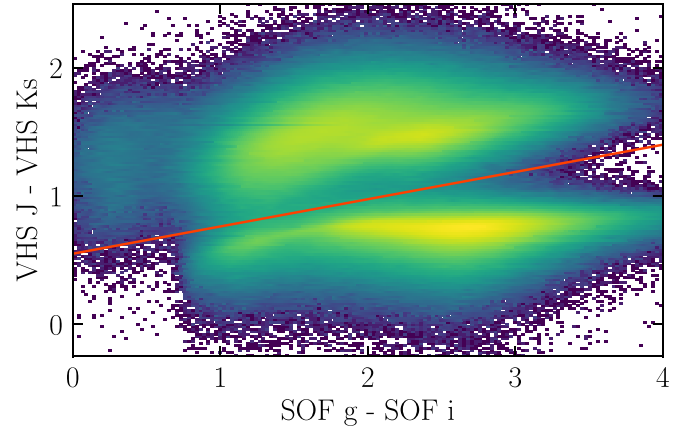
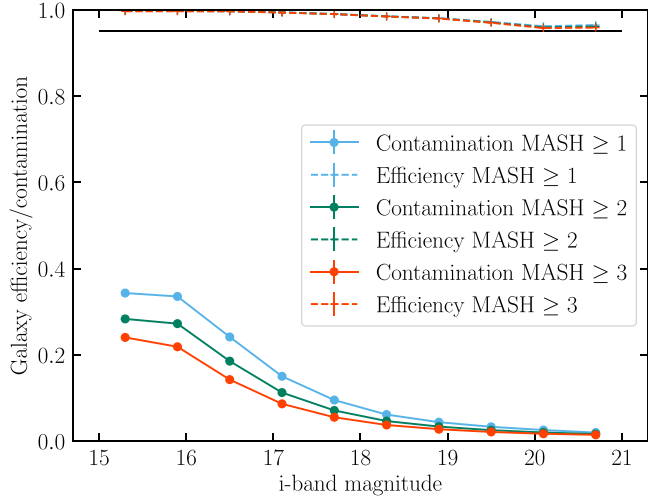


Figure 8. Optical DES vs. infrared VHS color distribution for star classification. The objects above the dividing line have galactic or QSO spectra. This color-based “truth” classification for Galactic and extragalactic populations is possible where VHS data are available and matched to DES sources, and is therefore limited to approximately $i < 21$.

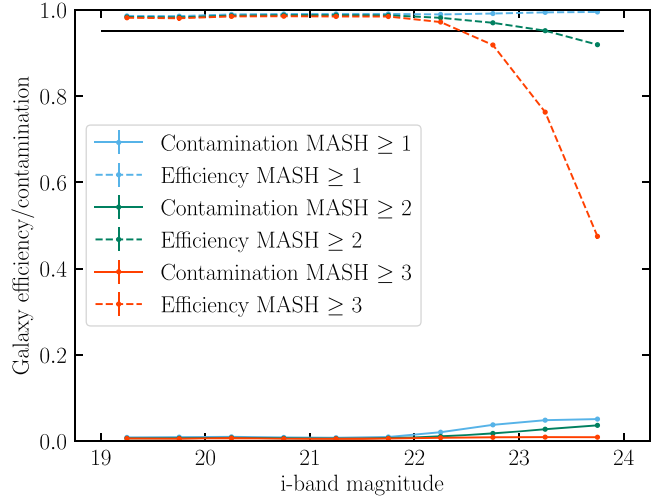
which overlaps the SN-X3 field. In Figure 9(b) we show the efficiency and purity of an extended source sample versus point sources. In this measurement, we estimate a 2% systematic error at fainter magnitudes due to classification errors in the reference catalog itself (as compared with space imaging).

From these figures, we can estimate that the galactic sample as defined by `EXTENDED_CLASS_MASH_SOF = 3` in the range of $i = [19, 22.5]$ will contain a contamination smaller than 2%. This range, for example, will contain most of the lens sample for the DES cosmologic analyses.

In Figure 10 we show the contamination level $(1 - \text{purity})$ for the stellar and galactic samples. The photometric redshift range considered is very important to consider when accounting for contamination from a stellar or extragalactic component. Stars will have a photometric redshift assigned as well and tend to accumulate at $\text{photo-}z \gtrsim 0.5$. This can impact the galactic sample specifically at bright magnitudes, where the



(a) Truth from VHS colors



(b) Truth from HSC morphology

Figure 9. Left: efficiency and contamination of point sources in different extended source samples using the VHS color selection as a reference. A large contamination at the bright end can be avoided by using infrared color selection and/or faint magnitude selection when the former is absent. Right: same measurements using the HSC-SSP DR2 catalog as a reference (see Section 3.2). Errors are 95% containment errors computed using a Bayesian approach for efficiencies as detailed in Paterno (2004), and cannot be visualized at this scale as they are $\sim 0.3\%$.

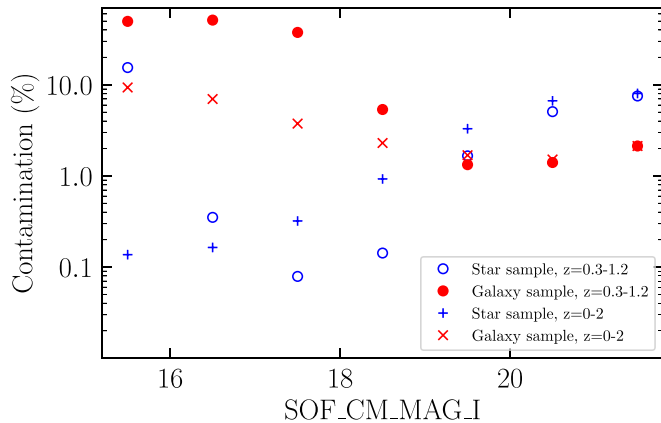


Figure 10. Impurity level in stellar and galactic samples as classified by EXTENDED_CLASS_MASH_SOFO (=0 or =3, respectively) for two photometric redshift ranges defined by DNF. Every object in the Y3 GOLD sample has a photometric redshift computed for them, including stars.

true star-to-galaxy ratio is higher, in this moderate photo- z range (see Crocce et al. 2019). The apparent extendedness of the contaminating stellar population is likely attributed to double stars in many cases. For the cosmology studies showcased in DES Collaboration (2018a) and Y3 analyses, the “source” and “lens” samples avoid this contamination through specific shape measurement codes and by removing bright objects, respectively. If one is interested in this bright regime however, additional color constraints or more sophisticated shape selections can help separate extended sources and double stars that have been merged into a single detection.

The EXTENDED_CLASS_MASH_SOFO classifier was built for general application based on the best options studied in Sevilla-Noarbe et al. (2018). Analyses in regions around foreground objects (such as globular clusters or the Magellanic Clouds) would test the performance of these morphological classifiers and/or build improved classifications with color information (Sevilla-Noarbe et al. 2018).

6.2. Object Quality Flag: FLAGS_GOLD

We use FLAGS_GOLD to indicate unusual characteristics of individual objects, including fitting failures and measurement anomalies. Flagged objects can be excluded as appropriate for a given analysis using bitwise operations. See Table 3 for a description of the various bits available per object.

6.3. Photometric Redshifts

Three standard photometric redshift codes were run on MOF and SOF photometries of Y3 GOLD objects ($griz$). We provide in this section a description of the estimates provided with Y3 GOLD, together with figures of merit describing their performance against an extensive collection of spectra, described in Gschwend et al. (2018). The reference catalog includes $\sim 2.2 \times 10^5$ spectra matched to DES objects from 24 different spectroscopic catalogs, most notably Sloan Digital Sky Survey (SDSS) DR14 (Abolfathi et al. 2018), DES’s own follow-up through the OzDES program (Lidman et al. 2020), and the VIMOS Extragalactic Redshift Survey (Garilli et al. 2014). Half of the spectra have been used for training the machine-learning methods, and the other half for the tests shown in this section. In all cases, point estimates and probability distribution functions of the samples can be computed. It is important to remark that cosmologic analyses making use of Y3 GOLD will often employ other approaches more suitable for the task at hand (see, e.g., Myles et al. 2020), with their own set of validation procedures. In this work, we present three approaches available in Y3 GOLD, with a measurement of bias and dispersion as a function of spectroscopic redshift using an extensive spectroscopic catalog.

6.3.1. Bayesian Photometric Redshifts, BPZ

The BPZ code uses a template-fitting approach where a collection of galactic SEDs are fit to the measured fluxes. The original code from Benítez (2000) has been modified for efficiency of execution as described in Hoyle et al. (2018) and incorporated into the DESDM system.

Table 3
Y3 GOLD FLAGS_GOLD Bit Flag Variable

| Flag Bit | No. of Objects Affected | Description |
|----------|-------------------------|---|
| 1 | 14185334 | MOF_FLAGS != 0 or MOF_FLAGS = NULL, flag raised by MOF processing |
| 2 | 6555347 | SOF_FLAGS != 0, flag raised by SOF processing |
| 4 | 1532648 | SOF_FLAGS == 1 or SOF_FLAGS > 2, flags for PSF fit failures |
| 8 | 746568 | Any SExtractor FLAGS_[GRIZ] > 3 |
| 16 | 3091171 | Any of IMAFLAGS_ISO_[GRIZ] != 0. ^a |
| 32 | 152999 | Bright blue artifacts in the images |
| 64 | 62653 | Bright objects with unphysical colors, possible transients |

Note.

^a The IMAFLAGS_ISO flag is set as an OR condition among the multiple pixels on multiple epochs composing the image, regarding a processing flag being set, according to the definition in Morganson et al. (2018).

BPZ has the capability of providing estimates for the redshifts from our knowledge of galactic spectra, up to high redshifts if needed, by modeling adequately their spectral evolution, thereby alleviating the need for expensive and biased measurements of spectroscopic sources for training sets. On the other hand, biases can arise in this case from inadequate calibration or incompleteness of the template base itself.

6.3.2. Directional Neighborhood Fitting Photometric Redshifts, DNF

DNF (De Vicente et al. 2016) creates an approximation of the redshift of objects through a nearest-neighbors fit of a hyperplane in color–magnitude space using a reference, or training set, from a large spectroscopic database.

DNF also provides a second redshift estimation as the nearest neighbor in the reference sample. This second estimation allows the method to replicate the science sample photo- z distribution, $N(z)$, under the assumption of training sample representativeness (see Hartley et al. 2020a for an exploration of this fact in machine-learning codes). Galaxies without close references in the training sample are tagged in this code.

This kind of solution offers an automatic incorporation of the subtleties of the photometric behavior of the system. In addition, some of the degeneracies in the photometry–redshift association can be detected as large differences between the two photo- z ’s provided by the method. However, the lack of representativeness of the training set as mentioned above is one of the major drawbacks of this kind of methodology.

6.3.3. Machine-learning Methods for Photometric Redshifts, ANNz2

ANNz2 (Sadeh et al. 2016) provides an alternative training-based photo- z estimate. ANNz2 is an updated version of the neural network code ANNz (Collister & Lahav 2004), and it differs from the latter by using several additional machine-learning methods beyond artificial neural networks, such as boosted decision trees (BDTs) and k -nearest-neighbors (k NN) algorithms.

For the Y3 Gold photo- z catalog, ANNz2 was run in randomized regression mode with 50 BDTs, using the same spectroscopic sample utilized for DNF, randomly split into training, and validation and testing sets. The estimate provided in the catalog results from the BDT with the best performance on the testing sample. The uncertainty is estimated through a k NN method, which takes into account the distance of galaxies in the Y3 sample from training galaxies in color space. As with DNF, an incomplete training set can introduce biases that need to be calibrated or accounted for.

6.3.4. Photo- z Performance Metrics

As a standard check on the performance of these photo- z codes, we present some quality metrics against the spectroscopic data set compiled as described in Gschwend et al. (2018). Figure 11 shows that the reconstructed estimation of the redshift is, in general, more accurate with DNF. At low redshifts ($z < 0.5$), the BPZ run available in Y3 GOLD shows poor performance, due to the adaptation of templates for better performance at high redshifts. In addition, we encounter some difficulties related to the lack of the u band to break some degeneracies among galaxy types and redshift at $z \sim 0.4$. We also show in Figure 12 that the impact of incorporating the chromatic corrections to photometric calibrations is negligible.

The point photo- z estimates shown here are mainly used for binning galactic samples. In Y3 cosmology, this is done for the magnitude-limited sample (Porredon et al. 2021) and the baryon acoustic oscillations sample (A. Carnero Rosell et al. 2021, in preparation). redMaGiC uses its own point estimate from the red-sequence template fitting (with a similar performance as DNF for those galaxies) as described in Rozo et al. (2016). The fiducial binning and redshift distributions of the source sample for the combined weak-lensing and large-scale structure analysis are described and validated in Myles et al. (2020).

In Figure 13 we show the comparison of the estimate of DNF against the spectroscopic redshift distribution on the validation sample, for illustration purposes. A qualitative agreement of the $N(z)$ estimate can be readily seen for the validation set used in this work.

7. Ancillary Maps

As with Y1 GOLD, the Y3 GOLD map products use HEALPix (Górski et al. 2005) as their base code, usually with an $nside = 4096$ resolution (approximately $0.86'$ across each pixel).

7.1. Footprint

The Y3 GOLD footprint is a geometric mask used to select regions of the survey with good coverage in multiple bands. While the complete Y3 GOLD object catalog contains all objects measured in the Y3A2 co-add processing (same objects as DR1 release; Section 3), only the subset of objects located within the Y3 GOLD footprint are considered as part of the DES Y3 cosmological analyses. We use the FLAGS_FOOTPRINT

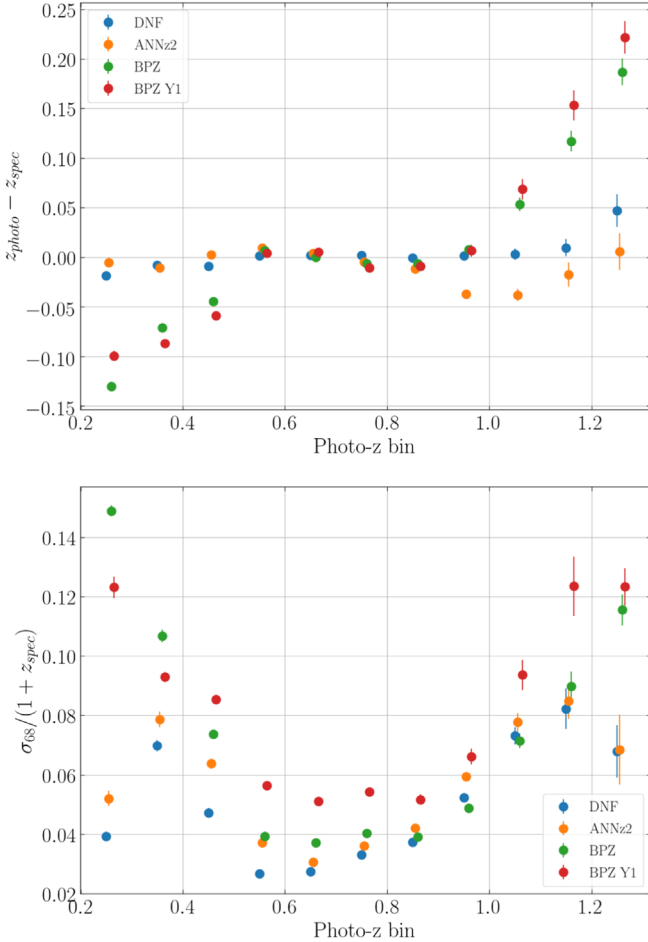


Figure 11. The residual of the point photometric redshift estimates (top) and the 68% quantile error using a test sample from a collected spectroscopic catalog (Gschwend et al. 2018), from BPZ, DNF, and ANNz2 (as well as Y1 GOLD BPZ). The lack of the u band limits precision at low redshifts. The training set is common between both machine-learning photo z codes. Although the test spectroscopic sample is quite extensive, collecting more than 100,000 spectra, it is not a statistically representative sample of Y3 GOLD.

variable to ensure consistency between the object catalog and Y3 GOLD footprint.

The minimum requirement for an object to be part of Y3 GOLD is summarized as follows:

1. At least one exposure on each band $griz$ is required in the object’s HEALPix pixel from the `NUM_IMAGE` map (Section 7.3).
2. At least 50% of overlapping coverage for each band is required in the `FRACDET` $griz$ map for that pixel as well (Section 7.3).
3. The object itself must have a value for the `NITER_MODEL` variable greater than zero for $griz$; that is, it must have been successfully fit to a model by `SEXTRACTOR` for the light profile in each of these bands.

In summary, these conditions require that the object must be in a HEALPix region with certain minimum observations, and that the object itself has been observed in the four bands in which `SOF` photometry is computed. Considering the detection fraction in each of the HEALPix pixels, the footprint area amounts to 4946 deg².

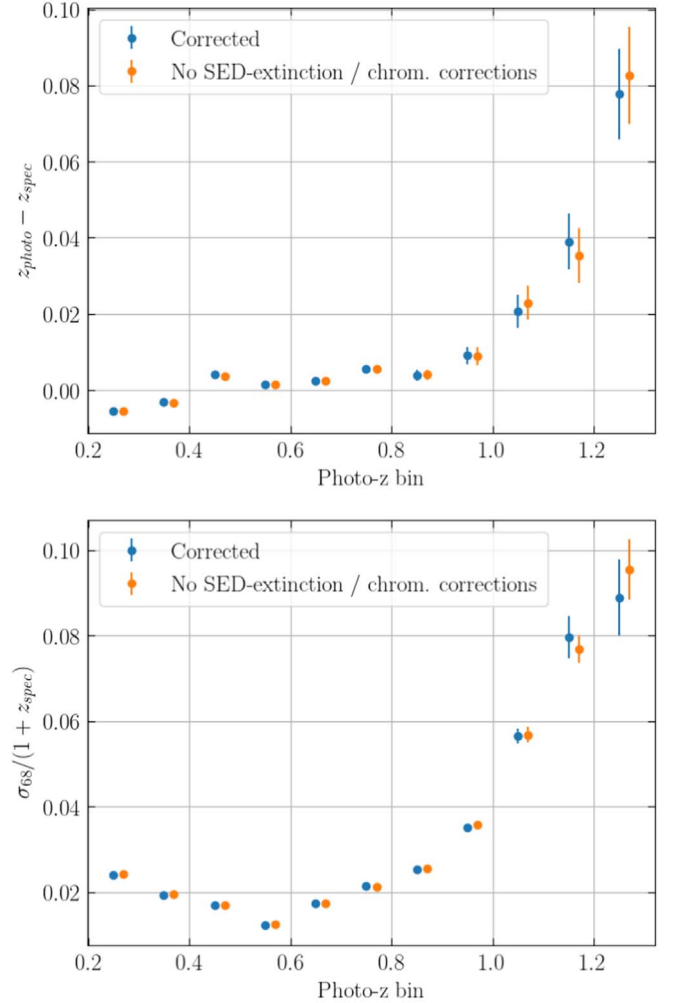


Figure 12. The residual of the point photometric redshift estimates (top) and the 68% quantile error over $(1 + z)$ (bottom) for DNF, with and without chromatic corrections. It can be seen that the impact in performance is negligible.

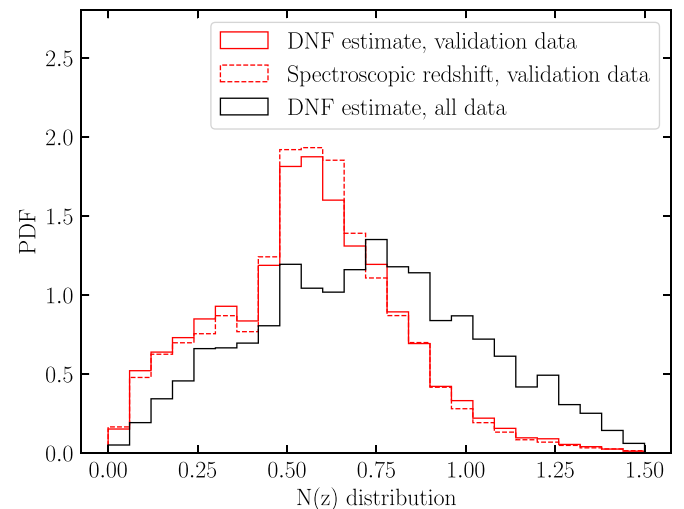


Figure 13. $N(z)$ comparison between DNF and the spectroscopic validation sample, as well as the distribution for a random sampling of Y3 GOLD. Selection included some basic quality cuts on `FLAGS_GOLD = 0` and `FLAGS_FOREGROUND < 2`, extended object selection (`EXTENDED_CLASS_MASH_SOF = 3`) and i -band magnitude range cut in the interval [17.5, 23.5].

Table 4
Y3 GOLD Foreground Region Mask

| Flag Bit | Area (deg ²) | Description |
|----------|--------------------------|---|
| 1 | 220.59 | 2MASS moderately bright star regions ($8 < J < 12$) |
| 2 | 22.63 | Large nearby galaxies (HyperLEDA catalog) |
| 4 | 91.12 | 2MASS bright star regions ($5 < J < 8$) |
| 8 | 100.61 | Region near the LMC |
| 16 | 86.51 | Yale bright star regions |
| 32 | 0.53 | Globular clusters |
| 64 | 61.13 | Brightest stars |

Note. Foreground mask for Y3 GOLD. The masked area from the Y3 GOLD catalog is calculated using the coverage fraction of the pixels that are removed from the footprint by each mask. The rationale for each mask can be found in Section 7.2.1.

7.2. Additional Masks

For most cosmologic analyses, we apply two additional geometric selections beyond the minimal “footprint” observability requirements (Section 7.1). These masks correspond to distinct types of effects: regions where nearby astrophysical objects hinder studies of distant galaxies (called “foreground regions”), and areas that are considered faulty from the measurement point of view, due to some deficiency in the source extraction or photometric measurement (“bad regions”; Fausti Neto et al. 2018).

In addition, we produce maps of survey properties and observing conditions (e.g., sky brightness, image quality) extracted from the set of single-epoch images that overlap each position in the survey.

7.2.1. Foreground Mask

Table 4 summarizes the mask bits and regions described in this section. Figure 14 shows the foreground mask. If a Y3 GOLD object is located within a HEALPix pixel that is part of one or more of the regions indicated in Table 4, the bit flag variable `FLAGS_FOREGROUND` is set using the corresponding bits. These are defined as follows:

1. Bit 1, 2MASS moderately bright stars: includes regions around stars with a J magnitude from the 2MASS (Skrutskie et al. 2006) catalog in the range $8 < J < 12$.
2. Bit 2, large nearby galaxies: this bit selects areas around large, nearby galaxies found in the HyperLEDA⁷⁴ catalog (Makarov et al. 2014).
3. Bit 4, 2MASS bright stars: same as bit 1 above, but including stars in the range $4 < J < 8$.
4. Bit 8, region near the LMC: this mask avoids the area with an overabundance of stars around the LMC, which can easily overwhelm the galactic catalog, or create heavy obscuration for cosmologic analyses.
5. Bit 16, Yale bright star catalog: approximately 1000 objects from the catalog overlap with the Y3 GOLD footprint. A linear function has been implemented to create a mask as a function with V-band magnitude from the catalog.
6. Bit 32, globular clusters: the list includes five globular clusters with magnitude $V < 10$, using the radius

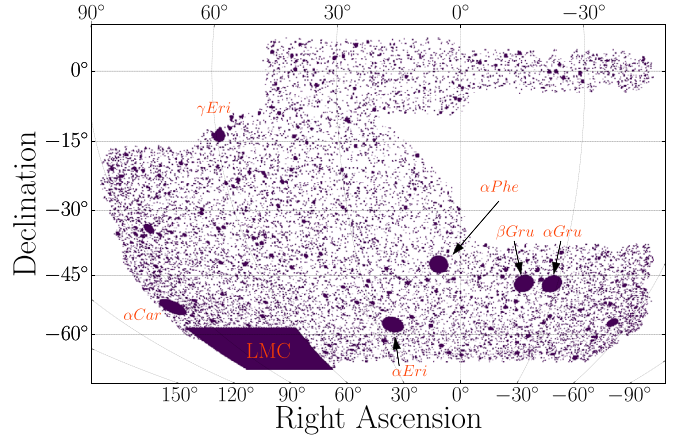


Figure 14. The foreground mask for Y3 GOLD, including all astrophysical objects that could hamper cosmological analyses (see the text for individual descriptions). The total area removed amounts to 551 deg². Note that the mask corresponding to bit = 1 (faint 2MASS stars) is not shown for clarity. Some of the largest individually masked areas (LMC, very bright stars) are pointed out as well with a text label.

Table 5
Very Bright Stars Exclusion List

| Name | α, δ | Radius (deg) |
|---------|-----------------------|--------------|
| α Phe | (6.5708, -42.3061) | 2.0 |
| α Eri | (24.4288, -57.2367) | 2.0 |
| γ Eri | (59.5075, -13.5086) | 1.5 |
| α Hyi | (29.6925, -61.5697) | 0.5 |
| α Col | (84.9121, -34.0741) | 1.0 |
| α Car | (95.9879, -52.6958) | 2.0 |
| α Pav | (306.41214, -56.7350) | 1.0 |
| α Gru | (332.0583, -46.9611) | 2.0 |
| β Gru | (340.6671, -46.8847) | 2.0 |
| Pi1 Gru | (335.6829, -45.9478) | 0.5 |
| P Dor | (69.1900, -62.0775) | 0.5 |

provided in the NGC2000 catalog.⁷⁶ These are NGC 1261, NGC 1851, NGC 7089, NGC 288, and NGC 1904.

7. Bit 64, very bright stars: these are 11 stars that produce large scattered light artifacts due to their brightness that go beyond the image masking and exclusion listing setup for the rest of the stars. A large radius is defined around them to remove areas with large densities of bright objects with anomalous colors. These stars are listed, including the exclusion radius, in Table 5.

7.2.2. Bad Regions Mask

Table 6 summarizes the mask bits and regions described in this section. As with the foregrounds, if a Y3 GOLD object is within a HEALPix pixel that is part of one or more of the regions indicated in Table 6, the bit flag variable `FLAGS_BADREGIONS` is set using the corresponding bits. These are described below:

1. Bit 1, co-add PSF failure regions: the co-addition process produces a discontinuous PSF function across the footprint that will corrupt SExtractor quantities that depend on the PSF such as `MAG_PSF` and `SPREAD_MODEL` (Desai et al. 2012; Bouy et al. 2013). Analyses

⁷⁴ <http://leda.univ-lyon1.fr/>

⁷⁵ <http://tdc-www.harvard.edu/catalogs/bsc5.html>

⁷⁶ <https://heasarc.gsfc.nasa.gov/W3Browse/all/ngc2000.html>

Table 6
Y3 GOLD Bad Region Mask

| Flag Bit | Area (deg ²) | Description |
|----------|--------------------------|-------------------------------------|
| 1 | 42.18 | Co-add PSF failure regions |
| 2 | 28.43 | Tiles with errors in MOF processing |
| 4 | 5.95 | High density of anomalous colors |

Note. Bad regions mask for Y3 GOLD. The masked area from the Y3 GOLD catalog is calculated using the coverage fraction of the pixels that are removed from the footprint by each mask. The rationale for each mask can be found in Section 7.2.2.

using these SExtractor quantities should mask out these regions.

2. Bit 2, tiles with errors in MOF processing: 66 DESDM “tiles” failed to finish processing the MOF pipeline. These problematic tiles are all associated with foreground objects and/or dense regions.
3. Bit 4, high density of anomalous colors: this mask is intended to remove reflections in the images, bad coverage of foreground galaxies, and a few satellite trails remaining in the images, using a selection on a high density of objects with extreme colors (with any color $g - r, r - i, i - z$ outside of the range $[-2, 3]$).

7.3. Survey Properties

We track the spatial variation of several observing conditions (see Table E1) across the survey footprint using mangle polygon masks (Section 3.1). Given that each location in the survey contains the information from a stack of images, a statistic (e.g., mean, minimum, maximum) is used to summarize this information as a scalar value for that location (Leistedt et al. 2016). This step is explained in Morganson et al. (2018).

The detailed geometry of the survey given by mangle is transformed into HEALPix maps for simplification and homogenization. In addition, bleed-trail and bright star masks for each band produced by DESDM are compacted into a single detection fraction HEALPix map (FRACDET), giving the effective coverage at each HEALPix pixel for each band. Furthermore, using the bleed-trail and bright star masks for any choice of bands $grizY$, we can also produce a combined detection fraction map. The HEALPix maps were produced using the DES science portal (Fausti Neto et al. 2018); the process is described in Appendix E.

DESDM delivered 27 survey properties for Y3 GOLD, together with bleed-trail and bright star masks for each band, totaling 135 mangle products for the entire survey (see Appendix E). Y3 GOLD provides pixelized versions of these survey property maps at HEALPix $nside = 4096$ resolution in NESTED ordering, as well as other useful maps used in cosmologic analyses such as the MOF, SOF, and MAG_AUTO depth maps described in Section 5, a stellar density map computed using “secure” stars, according to the EXTENDED_CLASS_MASH_SO_F classifier, and interstellar extinction maps.

8. Using Y3 GOLD

The Y3 GOLD data set will be released as was done with Y1 GOLD as an online resource, available at <https://des.ncsa.illinois.edu/releases>. This release includes the catalog itself, along with the maps detailed in Section 7 in HEALPix format.

The Y3 GOLD data set used for Y3 cosmologic analyses has internally been labeled as version 2.2. This version contains 399 million objects and 446 columns, which include the object ID, position, measured photometry and associated errors in each band using a variety of algorithms, shape information and errors, photometric redshifts and related quantities, and several flags (described in previous sections). We also provide the interstellar extinction in the direction of each object, as estimated from three different reddening maps (Schlegel et al. 1998; Lenz et al. 2017; Planck Collaboration 2014, see Appendix A.5).

We provide usage notes for the current Y3 GOLD version (to be updated for any subsequent versions produced). Some general recommendations are listed below.

1. The fundamental selection for Y3 GOLD is to select objects with `FLAGS_FOOTPRINT = 1`, as described in Section 7.1.
2. In general, the areas identified in Section 7.2.1 can present various problems in terms of photometry, junk objects, obscuration, etc., so the `FLAGS_FOREGROUND = 0` selection is generally recommended for extragalactic studies.
3. “Bad” regions coming from internal processing or data taking issues (Section 7.2.2) will vary depending on the choice of photometric pipeline. An SOF-based analysis can be safely done with `FLAGS_BADREGIONS < 4` whereas an MOF-based one should restrict to `FLAGS_BADREGIONS < 2`. A SExtractor-based analysis should use the bitwise AND operation (`FLAGS_BADREGIONS & 101 = 0`).
4. As explained in Section 6.2, `FLAGS_GOLD` allows for a selection of good-quality objects, by summarizing various flags and signatures of poor reconstructions in a single bitmask. However, Y3 GOLD provides the component flags from the different processes that were executed over the objects for more refined measurements. Typically, an SOF-based galactic sample would use the bitwise AND operation (`FLAGS_GOLD & 1111110 = 0`).
5. Photometry is provided as computed after FGCM calibration is applied, after atmospheric and instrumental corrections have taken place (i.e., top-of-the-atmosphere photometry). By default, cataloged magnitudes are not corrected for Galactic extinction. However a further zero-point correction based on Y4 imaging (with better quality) was computed prior to this release. In addition, as described in Section 4.3, a minor modification to take into account the spectral shape of the sources in the calibration plus the correction for Galactic extinction has to be applied to obtain the final top-of-the-Galaxy fluxes. Only the magnitudes and fluxes containing the `CORRECTED` suffix include these minor adjustments as well as Galactic extinction. For example, in the case of

Table 7
Example Selections from the Y3 GOLD Catalog, Provided for Illustrative Purposes

| Sample | Selection from Y3 GOLD Columns |
|--|---|
| High-purity galactic sample (SOF) | FLAGS_FOOTPRINT = 1 AND FLAGS_FOREGROUND = 0 AND (FLAGS_GOLD & 1111110) = 0 AND EXTENDED_CLASS_MASH_SOF = 3 AND SOF_CM_MAG_Corrected_I = [18,22.5] |
| High-purity galactic sample (MOF) | FLAGS_FOOTPRINT = 1 AND FLAGS_FOREGROUND = 0 AND (FLAGS_GOLD & 1111110) = 0 AND (FLAGS_BADREGIONS & 110) = 0 AND EXTENDED_CLASS_MASH_MOF = 3 AND MOF_CM_MAG_Corrected_I = [18,22.5] |
| High-purity galactic sample (SExtractor) | FLAGS_FOOTPRINT = 1 AND FLAGS_FOREGROUND = 0 AND (FLAGS_GOLD & 1111110) = 0 AND FLAGS_BADREGIONS = 0 AND EXTENDED_CLASS_COADD = 3 AND (MAG_AUTO_I + DELTA_MAG_Y4_I + DELTA_MAG_CHROM_I - A_SED_SFD98_I) = [18,22.5] |
| Basic object detections for subsequent shear studies | FLAGS_FOOTPRINT = 1 AND FLAGS_FOREGROUND = 0 AND (FLAGS_GOLD & 1111000) AND (FLAGS_BADREGIONS & 110) = 0 |
| High-purity stellar sample (SOF) | FLAGS_FOOTPRINT = 1 AND FLAGS_FOREGROUND = 0 AND (FLAGS_GOLD & 1111100) = 0 AND EXTENDED_CLASS_MASH_SOF <= 2 AND (SOF_PSF_MAG_R + DELTA_MAG_Y4_R + DELTA_MAG_CHROM_R - A_SED_SFD98_R) = [16,23] |
| High-completeness stellar sample (SOF) | FLAGS_FOOTPRINT = 1 AND FLAGS_FOREGROUND = 0 AND (FLAGS_GOLD & 1111100) = 0 AND EXTENDED_CLASS_MASH_SOFE <= 2 AND (SOF_PSF_MAG_R + DELTA_MAG_Y4_R + DELTA_MAG_CHROM_R - A_SED_SFD98_R) = [16, 23] |
| Red galactic sample | FLAGS_FOOTPRINT = 1 AND (FLAGS_FOREGROUND & 11111100) = 0 AND (FLAGS_GOLD & 1111110) = 0 AND EXTENDED_CLASS_MASH_SOF = 3 AND SOF_CM_MAG_Corrected_I = [17.5,22] AND SOF_CM_MAG_Corrected_I - SOF_CM_MAG_Corrected_Z + 2*(SOF_CM_MAG_Corrected_R - SOF_CM_MAG_Corrected_I) > 1.7 |

Note. Here “<&” corresponds to the bitwise AND operation.

magnitudes, this computation is:

$$\begin{aligned} \text{MAG_Corrected} = & \text{MAG} \\ & + \text{DELTA_MAG_Y4} \\ & + \text{DELTA_MAG_CHROM} \\ & - \text{A_SED_SFD98} \end{aligned} \quad (1)$$

(other extinction corrections may be applied as appropriate).

6. Only SExtractor Y -band photometry is available, as tests showed that incorporating this band into the overall multi-object fit degraded the performance in the rest of the bands.
7. The default recommended star–galaxy separation method to identify stars and galaxies is `EXTENDED_CLASS_MASH_SOF`. It is based in morphological quantities as described in Section 6.1. This method employs `EXTENDED_CLASS_SOF` as the main classifier for an object (see Table B1) but defaults to `EXTENDED_CLASS_WAVG`, available for the brighter objects, or `EXTENDED_CLASS_COADD` in case none of the others have been computed (in which case their values are set to a “sentinel” value). For cosmologic analyses, the selection `EXTENDED_CLASS_MASH_SOF = 3` is recommended, as it shows very low stellar contamination up to the magnitude limit, with a decrease in galactic selection efficiency only beyond $i > 22.5$. By exploring different ranges of `EXTENDED_CLASS` values, users can identify an appropriate sample for their science case. A default value of -9 is assigned when there is insufficient data available to compute the `EXTENDED_CLASS` variable.
8. At low redshifts ($z < 0.5$), the BPZ run available in this catalog shows poor metrics (Section 6.3); therefore, we recommend the usage of DNF or ANNz2 over BPZ in general.

In Table 7, some example queries are shown for illustrative purposes, to reflect the usage of flags and specific Y3 GOLD columns for a few typical situations.

9. Conclusions

The Y3 GOLD data set is the basic resource for cosmology using the Wide Survey of DES. It constitutes one of the largest galactic catalogs to date, and is the basis of a new set of results exploring the robustness of the Λ CDM model and its alternatives in exquisite detail. Beyond serving the immediate needs of the DES Collaboration, we hope that Y3 GOLD stimulates further analyses by the astronomy and cosmology community at large (as demonstrated by Asgari et al. 2019 and Cheng et al. 2020, for example). Data access tools and documentation are publicly available at <https://des.ncsa.illinois.edu/releases>. We highlight several notable features (Table 2) of this data set:

1. Sky coverage of nearly 5000 deg^2 in five photometric bands, $grizY$, at optical and near-infrared wavelengths;
2. $< 3 \text{ mmag}$ homogeneity using multi-epoch photometry and the FGCM calibration model;
3. Depths of 23.8, 23.6, 23.0, and 22.4 mag in $griz$ for extended objects at $S/N \sim 10$;
4. 399 million measured objects of which ~ 226 million are extended objects marked as “good” (very high galactic purity up to $i = 22.5$), prior to any flux or signal-to-noise selection;
5. Approximate coverage of $z \sim 0.2 - 1.2$ in photometric redshift.

Looking forward, the next major DES data processing campaign involves the full set of observations from the complete six seasons of DES, and an associated second public data release (DES DR2). DES Y6 data roughly double the integrated exposure time over most of the footprint (see Figure 2). In addition, several upgrades have been implemented in the science pipelines, including a lower S/N threshold for object detection, Gaia DR2 astrometric calibration, PSF modeling upgrades, and enhanced algorithms for the photometry of blended objects. The next generation of ground-based imaging surveys, including the Rubin Observatory LSST, will

require more stringent control of systematic uncertainties associated with galactic measurement and survey characterization (e.g., The LSST Dark Energy Science Collaboration 2018), motivating continued use of DES as a proving ground for new data reduction techniques and data products to support cosmological analyses.

K.B. acknowledges support from the U. S. Department of Energy, Office of Science, Office of High Energy Physics, under Award Nos. DE-SC0020278 and DE-SC0017647.

Funding for the DES Projects has been provided by the U. S. Department of Energy, the U. S. NSF, the Ministry of Science and Education of Spain, the Science and Technology Facilities Council of the United Kingdom, the Higher Education Funding Council for England, the National Center for Supercomputing Applications at the University of Illinois at Urbana-Champaign, the Kavli Institute of Cosmological Physics at the University of Chicago, the Center for Cosmology and Astro-Particle Physics at the Ohio State University, the Mitchell Institute for Fundamental Physics and Astronomy at Texas A&M University, Financiadora de Estudos e Projetos, Fundação Carlos Chagas Filho de Amparo à Pesquisa do Estado do Rio de Janeiro, Conselho Nacional de Desenvolvimento Científico e Tecnológico and the Ministério da Ciência, Tecnologia e Inovação, the Deutsche Forschungsgemeinschaft, and the Collaborating Institutions in the Dark Energy Survey.

The Collaborating Institutions are Argonne National Laboratory, the University of California at Santa Cruz, the University of Cambridge, Centro de Investigaciones Energéticas, Medioambientales y Tecnológicas-Madrid, the University of Chicago, University College London, the DES-Brazil Consortium, the University of Edinburgh, the Eidgenössische Technische Hochschule (ETH) Zürich, Fermi National Accelerator Laboratory, the University of Illinois at Urbana-Champaign, the Institut de Ciències de l’Espai (IEEC/CSIC), the Institut de Física d’Altes Energies, Lawrence Berkeley National Laboratory, the Ludwig-Maximilians Universität München and the associated Excellence Cluster Universe, the University of Michigan, NFS’s NOIRLab, the University of Nottingham, The Ohio State University, the University of Pennsylvania, the University of Portsmouth, SLAC National Accelerator Laboratory, Stanford University, the University of Sussex, Texas A&M University, and the OzDES Membership Consortium.

Based in part on observations at Cerro Tololo Inter-American Observatory at NSF’s NOIRLab (NOIRLab Prop. ID 2012B-0001; PI: J. Frieman), which is managed by the Association of Universities for Research in Astronomy (AURA) under a cooperative agreement with the NSF.

The DES data management system is supported by the NSF under grant Nos. AST-1138766 and AST-1536171. The DES participants from Spanish institutions are partially supported by MICINN under grants ESP2017-89838, PGC2018-094773, PGC2018-102021, SEV-2016-0588, SEV-2016-0597, and MDM-2015-0509, some of which include ERDF funds from the European Union. IFAE is partially funded by the CERCA program of the Generalitat de Catalunya. Research leading to these results has received funding from the European Research Council under the European Union’s Seventh Framework Program (FP7/2007-2013) including ERC grant agreements 240672, 291329, and 306478. We

acknowledge support from the Brazilian Instituto Nacional de Ciência e Tecnologia (INCT) do e-Universo (CNPq grant 465376/2014-2). A.C.R. acknowledges financial support from the Spanish Ministry of Science, Innovation and Universities (MICIU) under grant AYA2017-84061-P, co-financed by FEDER (European Regional Development Funds) and by the Spanish Space Research Program “Participation in the NISP instrument and preparation for the science of EUCLID” (ESP2017-84272-C2-1-R).

The Hyper Suprime-Cam (HSC) collaboration includes the astronomical communities of Japan and Taiwan, and Princeton University. The HSC instrumentation and software were developed by the National Astronomical Observatory of Japan (NAOJ), the Kavli Institute for the Physics and Mathematics of the universe (Kavli IPMU), the University of Tokyo, the High Energy Accelerator Research Organization (KEK), the Academia Sinica Institute for Astronomy and Astrophysics in Taiwan (ASIAA), and Princeton University. Funding was contributed by the FIRST program from Japanese Cabinet Office, the Ministry of Education, Culture, Sports, Science and Technology (MEXT), the Japan Society for the Promotion of Science (JSPS), Japan Science and Technology Agency (JST), the Toray Science Foundation, NAOJ, Kavli IPMU, KEK, ASIAA, and Princeton University.

Based (in part) on data collected at the Subaru Telescope and retrieved from the HSC data archive system, which is operated by Subaru Telescope and Astronomy Data Center at National Astronomical Observatory of Japan.

This paper makes use of software developed for the Vera Rubin Observatory LSST. We thank the LSST Project for making their code available as free software at <http://dm.lsst.org>. `healsparse` was developed under the Rubin Observatory LSST Dark Energy Science Collaboration (DESC) using LSST DESC resources.

This work has made use of data from the European Space Agency (ESA) mission Gaia (<https://www.cosmos.esa.int/gaia>), processed by the Gaia Data Processing and Analysis Consortium (DPAC, <https://www.cosmos.esa.int/web/gaia/dpac/consortium>). Funding for the DPAC has been provided by national institutions, in particular the institutions participating in the Gaia Multilateral Agreement.

This manuscript has been authored by Fermi Research Alliance, LLC under contract No. DE-AC02-07CH11359 with the U. S. Department of Energy, Office of Science, Office of High Energy Physics.

Facility: Blanco (DECam).

Software: SExtractor (Bertin & Arnouts 1996), PSFEx (Bertin 2011), SCAMP (Bertin 2006), SWarp (Bertin et al. 2002; Bertin 2010), mangle (Hamilton & Tegmark 2004; Swanson et al. 2008), HEALPix (Górski et al. 2005)⁷⁷, easyaccess (Carrasco Kind et al. 2019), astropy (Astropy Collaboration 2013), matplotlib (Hunter 2007), numpy (Van Der Walt et al. 2011), scipy (Virtanen et al. 2020), healpy,⁷⁸ fitsio,⁷⁹ ngmix (Sheldon 2014),⁸⁰ TOPCAT (Taylor 2005), `healsparse`,⁸¹ athena.⁸²

⁷⁷ <http://healpix.sourceforge.net>

⁷⁸ <https://github.com/healpy/healpy>

⁷⁹ <https://github.com/esheldon/fitsio>

⁸⁰ <https://github.com/esheldon/ngmix>

⁸¹ <https://healsparse.readthedocs.io/en/latest/>

⁸² <http://www.cosmostat.org/software/athena>

Appendix A

Unified Approach for Chromatic and Interstellar Extinction Corrections

We present a detailed formalism to apply SED-dependent photometric corrections to each source in the Y3 GOLD release. Building upon the work of Burke et al. (2018), our framework accounts for both chromatic corrections associated with the DECam bandpass (instrument and atmosphere) and interstellar extinction. We consider first the corrections for individual exposures, and then the corrections for multi-epoch photometry.

A.1. Single-epoch Corrections

Working forward along the path of light, the top-of-the-Galaxy (TOG) source spectrum incident at the Milky Way $F_\nu^{\text{TOG}}(\lambda)$ is reddened by interstellar dust before arriving at Earth. Consider a reddening law with optical index $a\tau(\lambda)$, where τ is normalized to $1\text{ }\mu\text{m}$. Let $a = f(\mathcal{E})$ be a normalization factor for the reddening law, where $\mathcal{E} \approx E(B - V)$ in the SFD98 prescription, but in general is some scaling from an external map providing the dust optical depth normalization. The dust-reddened top-of-the-atmosphere (TOA) source spectrum is $F_\nu^{\text{TOG}}(\lambda)e^{-a\tau(\lambda)}$.

The analog-to-digital (ADU) counts registered by the camera for a given band $b \in \{griY\}$ are proportional to the TOA source spectrum weighted by the transmission of the observed bandpass $S_b^{\text{obs}}(\lambda)$ integrated over wavelength.

$$\text{ADU}_b = \frac{A\Delta t}{gh} \int_0^\infty F_\nu^{\text{TOG}}(\lambda)e^{-a\tau(\lambda)}S_b^{\text{obs}}(\lambda)\lambda^{-1}d\lambda. \quad (\text{A1})$$

The instantaneous system throughput varies as a function of focal plane location and environmental conditions. The effective aperture A , exposure time Δt , gain g , and Planck's constant h appear as multiplicative factors.

We define three flux measurements of interest and the relationships between these measurements. The first is the TOA source spectrum as seen through the observed bandpass, i.e., the flux directly measured on the camera (Fukugita et al. 1996):

$$m_b^{\text{TOA,obs}} = -2.5 \log_{10} \left[\frac{\int_0^\infty F_\nu^{\text{TOG}}(\lambda)e^{-a\tau(\lambda)}S_b^{\text{obs}}(\lambda)\lambda^{-1}d\lambda}{\int_0^\infty F_\nu^{\text{AB}}S_b^{\text{obs}}(\lambda)\lambda^{-1}d\lambda} \right] \quad (\text{A2})$$

$$= -2.5 \log_{10} \left[\frac{gh\text{ADU}_b}{A\Delta t F^{\text{AB}} \int_0^\infty S_b^{\text{obs}}(\lambda)\lambda^{-1}d\lambda} \right] \quad (\text{A3})$$

$$= -2.5 \log_{10}(\text{ADU}_b) + 2.5 \log_{10}(\Delta t) + 2.5 \log_{10} \left(\int_0^\infty S_b^{\text{obs}}(\lambda)\lambda^{-1}d\lambda \right) + 2.5 \log_{10} \times \left(\frac{AF^{\text{AB}}}{gh} \right). \quad (\text{A4})$$

The magnitude is normalized relative to the AB scale with $F^{\text{AB}} = 3631\text{ Jy}$ (Oke & Gunn 1983). For a known observed bandpass, the measured ADU_b uniquely determines $m_b^{\text{TOA,obs}}$. In Y3 GOLD, the observed bandpass is provided by FGCM (Burke et al. 2018) for each individual CCD image together

with the zero-point in the AB magnitude system

$$ZP^{\text{AB}} = 2.5 \log_{10} \left(\frac{AF^{\text{AB}}}{gh} \right). \quad (\text{A5})$$

Second, we define the TOA source spectrum as seen through the DES standard bandpass:

$$m_b^{\text{TOA,std}} = -2.5 \log_{10} \left[\frac{\int_0^\infty F_\nu^{\text{TOG}}(\lambda)e^{-a\tau(\lambda)}S_b^{\text{std}}(\lambda)\lambda^{-1}d\lambda}{\int_0^\infty F_\nu^{\text{AB}}S_b^{\text{std}}(\lambda)\lambda^{-1}d\lambda} \right]. \quad (\text{A6})$$

The standard DES bandpass is defined as the instrument throughput averaged over CCDs and multiplied by the standard atmosphere. The difference between the TOA source spectrum seen through the observed and standard bandpass is the chromatic correction:

$$\begin{aligned} \delta m_b^{\text{chrom}} &= m_b^{\text{TOA,std}} - m_b^{\text{TOA,obs}} \\ &= -2.5 \log_{10} \left[\frac{\int_0^\infty S_b^{\text{obs}}(\lambda)\lambda^{-1}d\lambda}{\int_0^\infty S_b^{\text{std}}(\lambda)\lambda^{-1}d\lambda} \right] + 2.5 \log_{10} \\ &\quad \left[\frac{\int_0^\infty F_\nu^{\text{TOG}}(\lambda)e^{-a\tau(\lambda)}S_b^{\text{obs}}(\lambda)\lambda^{-1}d\lambda}{\int_0^\infty F_\nu^{\text{TOG}}(\lambda)e^{-a\tau(\lambda)}S_b^{\text{std}}(\lambda)\lambda^{-1}d\lambda} \right]. \end{aligned} \quad (\text{A7})$$

Third, we define the TOG source spectrum observed through the standard bandpass:

$$m_b^{\text{TOG,std}} = -2.5 \log_{10} \left[\frac{\int_0^\infty F_\nu^{\text{TOG}}(\lambda)S_b^{\text{std}}(\lambda)\lambda^{-1}d\lambda}{\int_0^\infty F_\nu^{\text{AB}}S_b^{\text{std}}(\lambda)\lambda^{-1}d\lambda} \right]. \quad (\text{A8})$$

The difference between the TOA and TOG source spectra observed through the standard bandpass is the interstellar extinction correction:

$$\begin{aligned} \delta m_b^{\text{extinction}} &= m_b^{\text{TOA,std}} - m_b^{\text{TOG,std}} = -2.5 \log_{10} \\ &\quad \left[\frac{\int_0^\infty F_\nu^{\text{TOG}}(\lambda)e^{-a\tau(\lambda)}S_b^{\text{std}}(\lambda)\lambda^{-1}d\lambda}{\int_0^\infty F_\nu^{\text{TOG}}(\lambda)S_b^{\text{std}}(\lambda)\lambda^{-1}d\lambda} \right]. \end{aligned} \quad (\text{A9})$$

This expression allows for computation of SED-dependent interstellar extinction corrections. Our expectation is that most science users will primarily use $m_b^{\text{TOG,std}}$ because this quantity is straightforward to compute for a given intrinsic source spectrum and allows for more direct comparisons of source photometry across the survey. Summarizing the results above, we can write the overall transformation from raw ADU counts to the chromatically correct and de-reddened magnitude as

$$m_b^{\text{TOG,std}} = m_b^{\text{TOA,obs}} + \delta m_b^{\text{chrom}} - \delta m_b^{\text{extinction}}. \quad (\text{A10})$$

The photometric corrections above require an SED template for each object, as described in Appendix A.4.

A.2. Multi-epoch Corrections

We now generalize Equation (A10) to the case of multi-epoch photometry. For the purpose of this derivation, we assume that the co-addition weighting is constant on a

per-object rather than a per-pixel basis. While this assumption is not precisely correct, most of the scaling in the SWarp co-addition is from the image-based zero-point weighting, rather than the local pixel-scale weighting. For WAVG catalog-co-add quantities, this assumption is correct because the weighting is done explicitly on the object level.

Suppose we have N observations of an object in band b that are enumerated with the index i . To simplify the subscripts, in this subsection we neglect the subscript b and assume we are working in band b . The raw multi-epoch magnitude $\langle m^{\text{obs}} \rangle$ is given by the weighted sum of individual measurements

$$\langle m^{\text{obs}} \rangle = \frac{\sum w_i m_i^{\text{obs}}}{\sum w_i}, \quad (\text{A11})$$

where w_i are the individual weights. For the weighted-average quantities, we use inverse-variance weights $w_i = 1/\sigma_i^2$, where σ_i is the single-epoch photometric error. For the co-add quantities, the weights are the median of the weight plane per amplifier for each observation. We can then apply per-observation-epoch photometric corrections δm_i to obtain the multi-epoch photometric corrected magnitude $\langle m^{\text{corrected}} \rangle$ as follows:

$$\langle m^{\text{corrected}} \rangle = \frac{\sum w_i (m_i^{\text{obs}} + \delta m_i)}{\sum w_i} \quad (\text{A12})$$

$$= \frac{\sum w_i m_i^{\text{obs}}}{\sum w_i} + \frac{\sum w_i \delta m_i}{\sum w_i} \quad (\text{A13})$$

$$= \langle m^{\text{obs}} \rangle + \frac{\sum w_i \delta m_i}{\sum w_i}. \quad (\text{A14})$$

For Y3 GOLD, we applied three per-observation-epoch corrections corresponding to a per-object chromatic correction, a gray zero-point correction, and a zero-point correction to shift to the AB magnitude scale:

$$\delta m_i = \delta m_i^{\text{chrom}} + \delta m_i^{\text{ZP,gray}} + \delta m_i^{\text{ZP,AB}}. \quad (\text{A15})$$

The per-observation-epoch chromatic corrections $\delta m_i^{\text{chrom}}$ come from Equation (A7). The gray zero-point corrections $\delta m_i^{\text{ZP,gray}}$ are described in Appendix A.3. The AB magnitude zero-point corrections $\delta m_i^{\text{ZP,AB}}$ arise due to an internal bookkeeping convention. Before we perform the co-addition, each individual image must be given a zero-point. With FGCM, zero-points are SED-dependent, but we do not know the per-object SEDs ahead of time, nor can we perform the co-addition with varying zero-points. The “native” FGCM SED is a flat $F_\nu(\lambda)$ spectrum in wavelength (AB magnitudes), but very few objects have this color. Therefore, we decided to make the co-adds based on a reference spectrum of a G star (our absolute calibrator star, C26202). In the database, the FGCM_ZPT value that is used for the co-adds is shifted to the AB magnitude spectrum, and the shift is recorded as FGCM_COADD_ZPTSHIFT. $\delta m_i^{\text{ZP,AB}}$ is obtained from the database as FGCM_COADD_ZPTSHIFT.

To apply these multi-epoch corrections to objects in Y3 GOLD, we computed the weighted average of each per-observation correction. Finally, the interstellar extinction correction $\delta m_b^{\text{extinction}}$ can be applied per-object (Appendix A.5) rather than per-observation, because we have defined the interstellar extinction correction in terms of the standard bandpass. The chromatic correction term (Equation (A7)) includes reddening. However,

Table A1
Summary of Multi-epoch Photometric Corrections

| Correction | Y3 GOLD column | Expression |
|-------------------------|-----------------|--|
| Gray and AB zero-point | DELTA_MAG_Y4 | $\langle \delta m_i^{\text{ZP}} \rangle = \frac{\sum w_i (\delta m_i^{\text{ZP,gray}} + \delta m_i^{\text{ZP,AB}})}{\sum w_i}$ |
| Chromatic | DELTA_MAG_CHROM | $\langle \delta m^{\text{chrom}} \rangle = \frac{\sum w_i \delta m_i^{\text{chrom}}}{\sum w_i}$ |
| Interstellar extinction | A_SED_SFD98 | $\delta m_b^{\text{extinction}}$ |

any changes in the assumed reddening law or reddening map would only cause second-order effects (especially in the low-extinction regime, which aptly describes most of the DES footprint), so we decided to keep the $e^{-a\pi(\lambda)}$ factor in Equation (A7) fixed to the fiducial prescription so that chromatic and interstellar extinction effects can be computed and tested independently. The multi-epoch magnitude for the TOG object spectrum observed through the standard bandpass is

$$\langle m^{\text{TOG,std}} \rangle = \langle m^{\text{obs}} \rangle + \langle \delta m_i^{\text{ZP}} \rangle + \langle \delta m^{\text{chrom}} \rangle - \delta m_b^{\text{extinction}}. \quad (\text{A16})$$

Table A1 summarizes the multi-epoch photometric corrections in the Y3 GOLD catalog, which can be applied as shown in Equation (1). We combine the multi-epoch corrections for the gray and AB magnitude zero-point corrections $\langle \delta m_i^{\text{ZP}} \rangle$ as DELTA_MAG_Y4 in the Y3 GOLD table:

$$\langle \delta m_i^{\text{ZP}} \rangle = \frac{\sum w_i (\delta m_i^{\text{ZP,gray}} + \delta m_i^{\text{ZP,AB}})}{\sum w_i}. \quad (\text{A17})$$

A.3. Updated Gray Zero-point Corrections in Y3 GOLD

There are several improvements to the “gray” SED-independent zero-points (E. S. Rykoff et al. 2021, in preparation) between the initial DES DR1 release and the Y3 GOLD release:

1. Aperture corrections in Y3 GOLD are performed internally during the calibration rather than as an afterburner step. Bernstein et al. (2018) found that photometric residuals between individual exposures within the same night could be primarily accounted for by improved aperture corrections. The Y3 GOLD calibration is based on SExtractor MAG_PSF photometry from FINAL-CUT processing and normalized to the flux measured within a 6" diameter aperture (MAG_APER_8).
2. The initial photometric calibration used for DR1 was based on a preliminary version of the DES standard bandpass. The updated Y3 GOLD calibration is now fully consistent with the DES Y3A2 standard bandpass publicly released with DR1.
3. The observational strategy of DES concentrated observations in two distinct halves of the final footprint during the first two years. It was only during the third year of DES that both halves were routinely observed within the same night. However, the third year of DES encountered unusually poor weather conditions. The Y3 GOLD photometric calibration incorporates a fourth year of observations to improve the uniformity across the full footprint

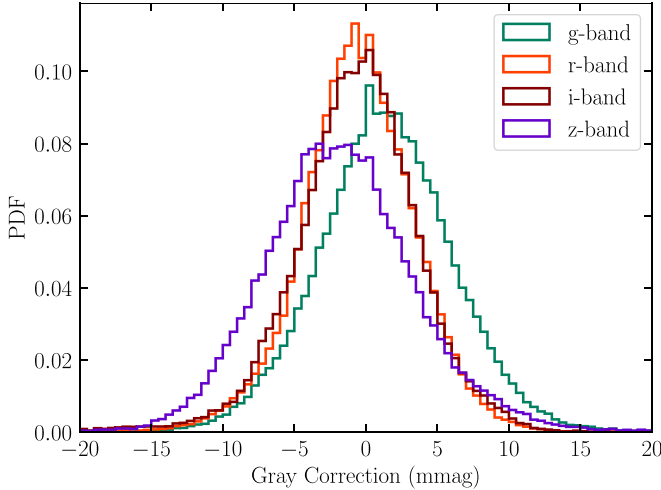


Figure A1. Distribution of multi-epoch zero-point corrections ($\langle \delta m_i^{\text{ZP}} \rangle$) that apply to the Y3 GOLD release, updated since the DR1 release.

(for the purpose of photometric calibration only; no Y4 imaging was included in the co-add).

4. We did not use GPS as input to the water vapor term in FGCM for the Y3 GOLD calibration, as this GPS input was compromised during a period of the Y1–Y3 observations, and led to spatially coherent photometric residuals in the z band over a small region of the footprint.
5. Technical improvements to the fitting procedure in the FGCM code have improved the overall stability of the calibration.

The distribution of updated zero-point corrections ($\langle \delta m_i^{\text{ZP}} \rangle$, which include both the AB magnitude and updated gray zero-point corrections per Equation (A17), is plotted in Figure A1.

A.4. Estimating Per-object Template SEDs: $F_{\nu}(\lambda)$

We compute photometric corrections for every co-add object as a function of its spectral type, as defined by their colors, to account for the differences relative to the FGCM reference spectrum.

Except in special cases (in particular SNe Ia), we generally do not know and/or do not want to assume an intrinsic spectrum of a given source. Therefore, we must decide which source spectrum to use when computing chromatic corrections. One could take an empirical approach and derive a linearized source spectrum directly from DES data, but this is problematic in bands at the boundaries of DES wavelength coverage (i.e., g and Y) and for drop-outs, since the color is not well constrained. We instead identify a best-fit realistic spectrum as a first step of the chromatic corrections described above.

We divide sources into two sets: (1) clearly identified stars, and (2) galaxies + ambiguous sources, which will mainly be faint galaxies. For the secure stars, flux measurements in two or more bands are sufficient to identify a template source spectrum, since the stellar locus is narrow and approximately monotonic in color. We use the Pickles (1998) stellar spectral library taken from the `big-macs-calibrate` code,⁸³ augmented with the bluest spectral templates from the original library. The `big-macs-calibrate` library does not cover

the full range of stellar colors; however, its template library has some important advantages since the spectral resolution is increased relative to the initial library, reducing the scatter considerably for the reddish M stars. Secure stars are selected as follows:

```
WHERE (((mag_auto_r BETWEEN 5. AND 22.0)
AND abs(wavg_spread_model_r) < 0.003)
OR ((mag_auto_i BETWEEN 5. AND 22.0)
AND abs(wavg_spread_model_i) < 0.003)
OR
((mag_auto_r BETWEEN 5. AND 20.0)
AND abs(spread_model_r) < 0.005
AND abs(spread_model_i) < 0.005));
```

For galaxies, we use the COSMOS SED library and run the LePhare photo- z code to identify a best-fit spectral template and redshift for each individual source. The initial fit uses the standard DES bandpass and fiducial reddening correction (Appendix A.5). Even if the initial best-fit spectrum is not fully accurate, the shape will be constrained at the level allowed by DES data alone. At this stage, the specific value of the best-fit galactic redshift is actually not important, so long as the best-fit spectral *shape* is approximately correct.

The COSMOS galactic SED library was chosen based on agreement between the colors of the templates and measured colors of the Y3 GOLD galactic sample, as seen in Figure A2. Various tests indicated that alternative choices of SED library provided suboptimal color matching, as they did not overlap some regions of color space occupied by the Y3 GOLD galaxies. We verified, using a random subsample, that the colors of the best-fit SEDs are not biased relative to the Y3 GOLD colors, as seen in Figure A3. The shape of the SEDs correctly represents the *griz* colors of sources for all spectral types in the galactic sample.

Figure A4 shows the range of SED templates considered for both stars and galaxies, as well as the flat $F_{\nu}(\lambda)$ spectrum, used as a reference for the fiducial interstellar extinction correction (Appendix A.5).

In Figure A5 we show the distribution of chromatic corrections for the *griz* bands. Even though chromatic corrections improve the photometric calibration and are therefore applied to Y3 GOLD, its effect is typically at the millimagnitude level. Also, we measured a negligible effect when we measured the effect of chromatic corrections on the recovered cosmological parameters on supernova science (Lasker et al. 2019), or as we saw in internal tests when estimating the photometric redshifts against a validation sample (Section 6.3).

Chromatic corrections are needed when two conditions are both met: (1) the observed passband differs from the standard passband and (2) the object SED is different from the reference SED. Most objects differ from the flat $F_{\nu}(\lambda)$ reference spectrum adopted for Y3 processing, and chromatic corrections can be tens of millimagnitudes in individual DECam exposures (Burke et al. 2018). However, chromatic corrections are reduced in the co-add as the number of exposures increases, because one typically averages over observing conditions, and the observed passband approaches the standard passband. By contrast, SED-dependent effects do not average down for interstellar extinction.

⁸³ <https://github.com/patkel/big-macs-calibrate>

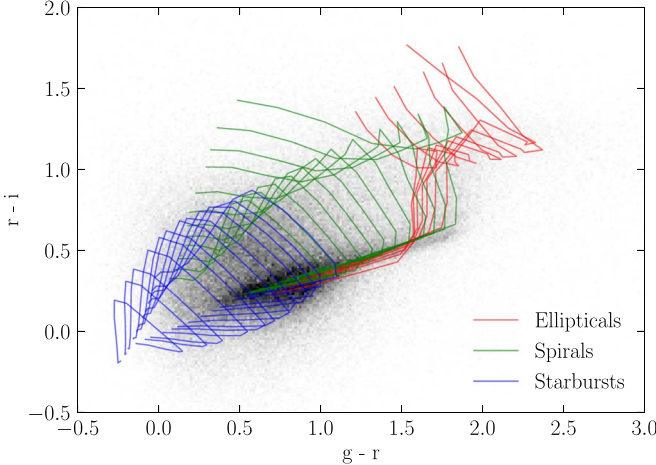


Figure A2. DES Y3 GOLD galactic photometry (SOF; black points) compared to predicted DECam colors for 31 COSMOS SED tracks (Ilbert et al. 2009). Each track represents a range in redshift, and is colored by galaxy type. Of the various galactic SED libraries considered, COSMOS had the highest overlap with the observed Y3 GOLD galactic color locus.

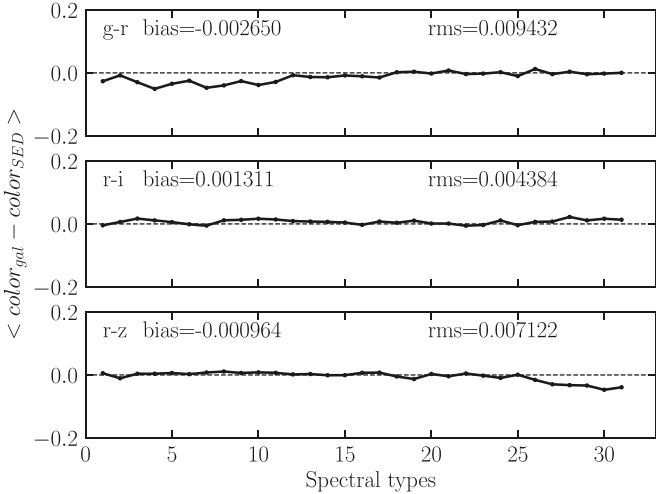


Figure A3. Mean difference between the colors of DES Y3 GOLD and the colors of the best-fit SED as a function of SED, for a subsample of galaxies. In general, there is an excellent agreement.

A.5. Interstellar Extinction Corrections

In general, both $\tau(\lambda)$ and a vary between lines of sight through the Galaxy. For our fiducial interstellar extinction correction, we will treat the reddening law $\tau(\lambda)$ as invariant with respect to Galactic coordinates over the DES footprint.

To obtain de-reddened (TOG) photometry, per-object corrections corresponding to four interstellar extinction models are delivered with Y3 GOLD: one “fiducial” SED-independent interstellar extinction based on the $E(B - V)$ reddening map of Schlegel et al. (1998, SFD98), and three SED-dependent models based on the reddening maps of SFD98, Planck Collaboration (2014), and Lenz et al. (2017), respectively. The reddening maps of SFD98 and Planck Collaboration (2014) estimate the dust column density based on thermal emission, whereas Lenz et al. (2017) use the 21 cm emission of neutral hydrogen in our Galaxy as a dust proxy.

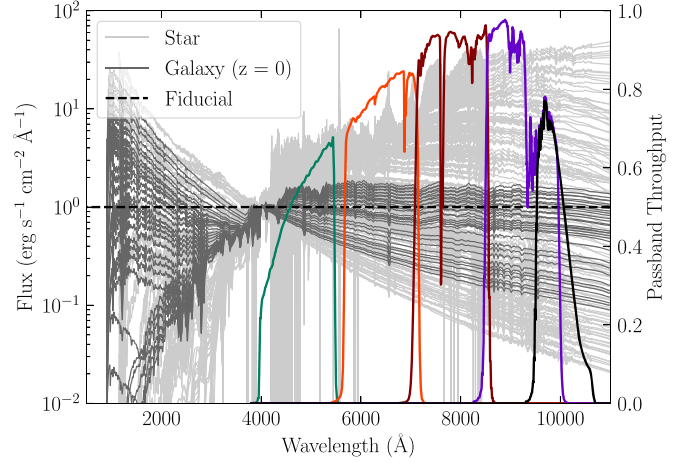


Figure A4. Spectral libraries used for chromatic corrections and SED-dependent interstellar extinction corrections. The galactic and stellar SEDs are compared to a constant $F_\lambda(\lambda)$ spectrum, used as the reference for the fiducial interstellar extinction correction. For galaxies, we use the COSMOS SED collection from Ilbert et al. (2009), and the Pickles (1998) library for stars. In addition, we also show the DES spectral passbands covering from 4000 to 12000 Å.

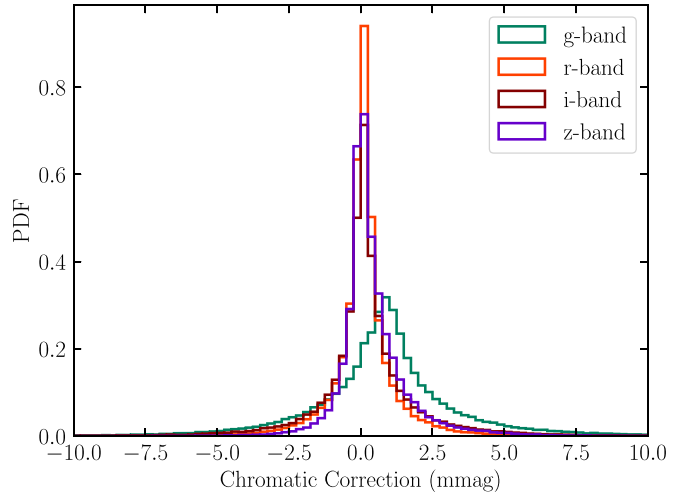


Figure A5. Distribution of chromatic corrections for $griz$ bands for a subsample of Y3 GOLD. Compared with the gray zero-point corrections (Figure A1), these are of smaller amplitude.

For the fiducial model, we assume a flat reference spectrum in $F_\lambda(\lambda)$ (i.e., constant value in units of $\text{erg s}^{-1} \text{cm}^{-2} \text{Å}^{-1}$), which is roughly centered within the color space of stellar and galactic SED templates (see Figure A4). For the three SED-dependent models, we use the same per-object SED template identified for chromatic corrections. We use the DES Y3A2 standard bandpass, and for each model, we adopt a Fitzpatrick (1999) reddening law with $R_V = 3.1$, consistent with the $E(B - V)$ map usage recommendations. We consider a low-extinction limit for which the correction is linear with respect to $E(B - V)$ values. Following Schlafly & Finkbeiner (2011), we rescale the SFD98 reddening map by a factor $N = 0.78$.

The values of the SED-dependent extinction correction for stars and galaxies are shown in Figures A6 and A7. Figure A8 shows the distribution of color residuals between several choices of reddening maps relative to SFD98.

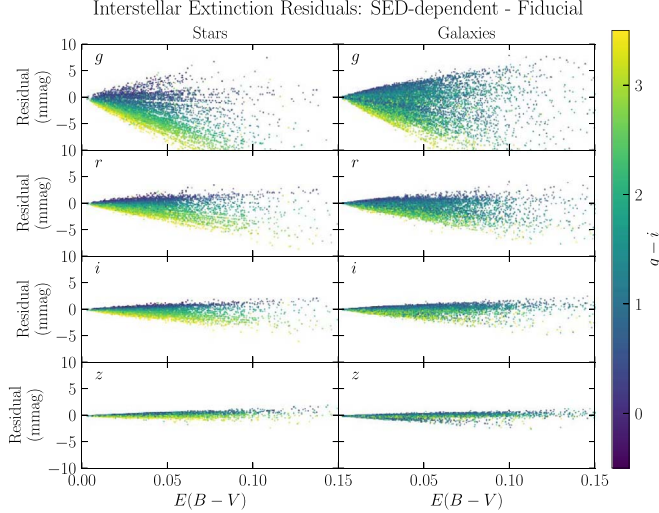


Figure A6. SED-dependent interstellar extinction corrections by band.

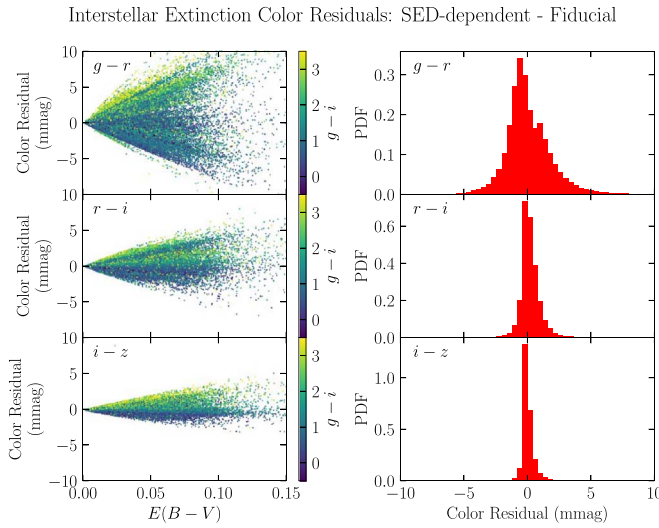


Figure A7. SED-dependent interstellar extinction corrections by color.

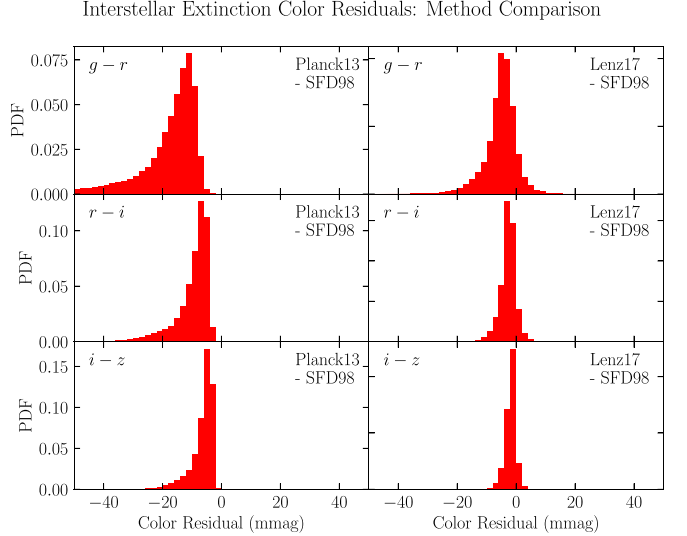


Figure A8. Color residuals between several extinction $E(B-V)$ maps (Lenz et al. 2017; Planck Collaboration 2014) and our fiducial choice, SFD98 (Schlegel et al. 1998).

Appendix B The EXTENDED Object Classifiers

The EXTENDED object classifiers were specifically designed for the Y3 GOLD release. Different flavors correspond to different usages of shape-related quantities from the Y3 GOLD data set, including SExtractor variables, ngmix-based, or both. All of these classifiers are built according to the same logical structure, using the following equation:

$$\text{EXTENDED_CLASS} = \sum_{i=1}^3 [\text{var} + E_i \cdot \text{varerr} > \text{th}_i] \quad (\text{B1})$$

where var and varerr correspond to a specific morphological variable and its error, and the values E_i , th_i are obtained according to the performance of the classifier against deeper imaging. For a given object, each time the condition is met in the summation in Equation (B1), a unit is added to EXTENDED_CLASS, therefore obtaining an integer value

Table B1
EXTENDED_CLASS Detailed Description, Including Input Variables and Parameter Values

| Classifier Name | <i>var</i> | <i>varerr</i> | $E_{1,2,3}$ | $th_{1,2,3}$ |
|----------------------|-------------------|----------------------|-------------|---------------------|
| EXTENDED_CLASS_SOF | SOF_CM_T | SOF_CM_T_ERR | (5,1,-1) | (0.1,0.05,0.02) |
| EXTENDED_CLASS_MOF | MOF_CM_T | MOF_CM_T_ERR | (5,1,-1) | (0.1,0.05,0.02) |
| EXTENDED_CLASS_COADD | SPREAD_MODEL | SPREADERR_MODEL | (3,1,-1) | (0.005,0.003,0.001) |
| EXTENDED_CLASS_WAVG | WAVG_SPREAD_MODEL | WAVG_SPREADERR_MODEL | (3,1,-1) | (0.005,0.003,0.001) |

Note. See Equation (B1) for details on the expression. EXTENDED_CLASS_SOF and EXTENDED_CLASS_MOF have essentially the same performance. SPREAD_MODEL and SPREADERR_MODEL are SExtractor outputs described in Desai et al. (2012) and Bouy et al. (2013).

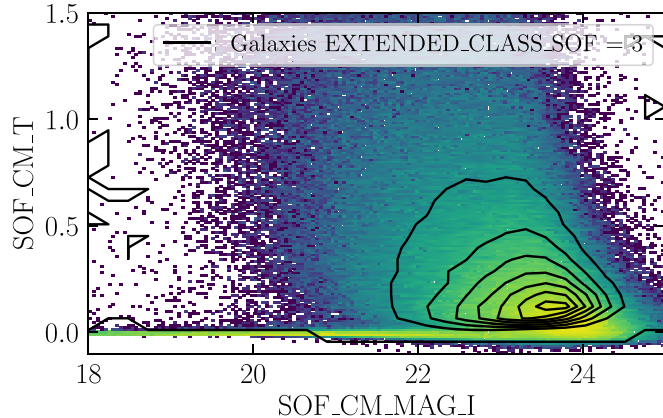


Figure B1. The distribution of SOF_CM_T, the basis for the EXTENDED_CLASS_MASH_SOF classifier, is shown as a function of magnitude. The heatmap shows the overall distribution of objects, whereas the contour lines indicate where the objects selected as galaxies (EXTENDED_CLASS_MASH_SOF = 3) lie in this parameter space.

between 0 and 3. The parameters E_i , th_i are chosen so that larger numbers correspond to more secure extended objects, whereas lower numbers correspond, more likely, to point-like objects. EXTENDED_CLASS = 0 indicates high-confidence stars and QSOs. When *var* cannot be computed for the particular object, a default value of EXTENDED_CLASS = -9 is assigned. In Table B1 we provide the specific parameters used for each classifier in Y3 GOLD. The “MASH” variants default to EXTENDED_CLASS_COADD for those objects with unavailable SOF or MOF information.

The distribution of SOF_CM_T, the basis for the EXTENDED_CLASS_MASH_SOF classifier, is shown as a function of magnitude in Figure B1.

Appendix C Main Catalog Columns

In Table C1 we summarize the essential columns of the Y3 GOLD data set with their brief description. Full details will be provided upon release at <https://des.ncsa.illinois.edu/releases/>.

Table C1
Selected Y3 GOLD Catalog Columns

| Y3 GOLD Catalog Column Family | Units | Description |
|---|---|---|
| COADD_OBJECT_ID | | Unique identifier for a Y3 co-add object |
| RA, DEC, B, L | Degrees | Equatorial and Galactic coordinates |
| ALPHAWIN_J2000, DELTAWIN_J2000 | Degrees | Equatorial coordinates using a Gaussian-windowed measurement (for precise astrometry) |
| (SOF/MOF)_(CM/PSF)_(MAG/FLUX)_(GRIZ) | Magnitudes or counts per second (MAG or FLUX) | Photometry as measured by the multi-epoch, multiband pipeline defined in Section 3.3, for a composite galactic model or a PSF-like one |
| (SOF/MOF)_(CM/PSF)_(MAG/FLUX)_ERR_(GRIZ) | Magnitudes or counts per second (MAG or FLUX) | Estimated error for the above |
| A_FIDUCIAL_(GRIZY) | Magnitudes | SED-independent interstellar extinction based on the $E(B - V)$ reddening map of Schlegel et al. (1998, SFD98) |
| A_SED_(SFD98/LENZ13/PLANCK17)_(GRIZY) | Magnitudes | SED-dependent interstellar extinction based on the $E(B - V)$ reddening maps of Schlegel et al. (1998), Lenz et al. (2017), and Planck Collaboration (2014) |
| DELTA_MAG_CHROM_(GRIZY) | Magnitudes | Co-add-object chromatic correction |
| DELTA_MAG_Y4_(GRIZY) | Magnitudes | Updates to photometry from Y4 imaging |
| (SOF/MOF)_CM_MAG_Corrected_(GRIZ) | Magnitudes or counts per second (MAG or FLUX) | Corrected CM_MAG quantities: (SOF/MOF)_CM_MAG_(GRIZ) + DELTA_MAG_Y4_(GRIZ) + + DELTA_MAG_CHROM_(GRIZ) - A_SED_SFD98_(GRIZ) |
| (SOF/MOF)_CM_T | arcsec ² | Size squared of the object: $T = \langle x^2 \rangle + \langle y^2 \rangle$ |
| (SOF/MOF)_CM_T_ERR | arcsec ² | Estimate of error in CM_T |
| EXTENDED_CLASS_MASH_(SOF/MOF) | | Classification code for the “extendedness” of object, from 0 (point-like) to 3 (extended-like) |
| FLAGS_FOOTPRINT | | Flag indicating that the object belongs to Y3 GOLD |
| FLAGS_GOLD | | Flag showing possible processing issues with the object |
| FLAGS_FOREGROUND | | Flag showing that the object is in the area of influence of a foreground object from an imaging point of view |
| FLAGS_BADREGIONS | | Flag showing that the object is in an area with generalized issues in processing or data quality |
| DNF_(ZMC/ZMEAN/ZSIGMA)_(MOF/SOF) | | DNF photo z statistics for the object |
| BPZ_(ZMC/ZMEAN/ZMODE/ZSIGMA/ZSIGMA68)_(MOF/SOF) | | BPZ photo z statistics for the object |
| BPZ_TEMPLATE_ID_(MOF/SOF) | | BPZ template identifier |

Note. Names in parentheses show options for a given type of column separated by slashes for each column. In addition several `SEextractor` quantities are available as well. Full details at <https://des.ncsa.illinois.edu/releases>.

Appendix D Photometric Transformation Equations with Other Systems

In this Appendix, we present transformation equations based on SDSS DR13 and DES Y3A1_FINALCUT single-epoch data⁸⁴ (Stringer et al. 2019). The zero-point (the constant term) in each relation was derived by comparing the observed SDSS DR13 versus Y3A1_FINALCUT relation with its Pickles (1998) synthetic counterpart, and then manually refining the zero-point (the constant term) to match the calibration of the Y3A1_FINALCUT FGCM standard stars (v2.5).

The ugr transformations apply for stars with $0.2 \leq (g - r)_{\text{sdssdr13}} < 1.2$. The izY transformations apply for stars with $0.0 \leq (i - z)_{\text{sdssdr13}} < 0.8$.

$$\begin{aligned}
 u_{\text{des}} &= u_{\text{sdssdr13}} - 0.479 + 0.466 \\
 &\quad \times (g - r)_{\text{sdssdr13}} - 0.350 \times (g - r)_{\text{sdssdr13}}^2 \quad (D1) \\
 g_{\text{des}} &= g_{\text{sdssdr13}} + 0.001 - 0.075 \times (g - r)_{\text{sdssdr13}} \quad (D2) \\
 r_{\text{des}} &= r_{\text{sdssdr13}} - 0.009 - 0.069 \times (g - r)_{\text{sdssdr13}} \quad (D3) \\
 i_{\text{des}} &= i_{\text{sdssdr13}} + 0.014 - 0.214 \times (i - z)_{\text{sdssdr13}} \\
 &\quad - 0.096 \times (i - z)_{\text{sdssdr13}}^2 \quad (D4)
 \end{aligned}$$

$$z_{\text{des}} = z_{\text{sdssdr13}} + 0.022 - 0.068 \times (i - z)_{\text{sdssdr13}} \quad (D5)$$

$$Y_{\text{des}} = z_{\text{sdssdr13}} + 0.045 - 0.306 \times (i - z)_{\text{sdssdr13}} \quad (D6)$$

with errors expressed in rms being $\text{rms}_u = 0.055$, $\text{rms}_g = 0.021$, $\text{rms}_r = 0.021$, $\text{rms}_i = 0.023$, $\text{rms}_z = 0.025$, and $\text{rms}_Y = 0.030$ for stars in this color range.

We also provide here the transformation equations with HSC-SSP DR2 for the *griz* bands (available for our default SOF photometry). In this case, we adopted a simpler approach by which we downloaded a bright sample of stars from the HSC-SSP DR2 catalog, and matched positionally to the corresponding Y3 GOLD stars, as defined by `EXTENDED_CLASS_MASH_SO` = 0. In this way, we obtain the following fitted coefficients:

$$g_{\text{des}} = g_{\text{hscdr2}} + 0.011490 - 0.0167 \times (g - r)_{\text{hscdr2}} \quad (D7)$$

$$r_{\text{des}} = r_{\text{hscdr2}} - 0.015233 - 0.127021 \times (r - i)_{\text{hscdr2}} \quad (D8)$$

$$i_{\text{des}} = i_{\text{hscdr2}} - 0.002067 - 0.12845 \times (i - z)_{\text{hscdr2}} \quad (D9)$$

$$z_{\text{des}} = z_{\text{hscdr2}} + 0.006933 - 0.31025 \times (z - Y)_{\text{hscdr2}} \quad (D10)$$

⁸⁴ <http://www.ctio.noao.edu/noao/node/5828#transformations>

Appendix E

Survey Property Maps

Survey property maps are computed from a base mangle polygon file and converted to HEALPix maps as follows for each quantity. First we divided the sky in HEALPix pixels with $nside = 32768$, which corresponds to 1.61×10^9 pixels in the DES footprint ($0.01 \text{ arcsec}^2/\text{pix}$). Then, for each of these pixels, given the R.A. and decl. of the pixel center, we look into the `mangle` mask to obtain the value of the physical quantity of interest at the given position. With this, we have pixelized the `mangle` mask to a resolution of $nside = 32768$. From here, we downgrade the resolution to the desired final $nside$. For Y3, we select $nside = 4096$ as our default choice ($0.738 \text{ arcmin}^2/\text{pix}$). To do this, we average the values of the 64 smaller pixels that are contained into one $nside = 4096$ pixel (for a visual interpretation of this process, we refer the reader to Figure 9 in Drlica-Wagner et al. 2018).

The FRACDET maps are assembled in a similar fashion, but using star and bleed-trail masks as the source for information on regions in the sky that have been compromised in the

images. At $nside = 32768$, whenever a pixel is not contained in the magnitude limit map (consider it as the observation map), or masked by a bright star or a bleed-trail, the small pixel is given an UNSEEN value. Then, each $nside = 4096$ pixel takes a value corresponding to the fraction of pixels that have been observed, for example, from the 64 higher-resolution pixels within. In the combined coverage map, when we use many bands, `griz` or `grizY`, the bleed-trail and bright star masks are combined at the level of $nside = 32768$, where in this resolution, we impose detection in all of the given bands. If any of the selected bands is UNSEEN, then that sub-pixel will be set to UNSEEN.

In Table E1 we summarize the observing conditions per band. We also include commonly used survey property maps in each band. Figures E1–E6 show these maps as a function of position in the sky and the corresponding histogram of computed values for these positions (computed in $nside = 4096$ HEALPix resolution). Note that the linear features along equal R.A. values are a consequence of the observational strategy to ensure a complete tiling of the sphere.

Table E1
Y3 GOLD Survey Properties

| DES Map Name | Units | Description |
|------------------------------|------------------------------------|---|
| NUMIMAGE | | Number of images |
| MAGLIM | | Magnitude limit estimated by <code>mangle</code> from the weight maps ^a |
| FRACDET | | Effective area fraction considering the bleed-trail and bright star masks |
| EXPTIME.SUM | seconds | Exposure time |
| T_EFF.(WMEAN/MAX/MIN) | | Figure of merit for quality of observations t_{eff} ^b |
| T_EFF_EXPTIME.SUM | seconds | Exposure time multiplied by t_{eff} |
| SKYBRUTE.WMEAN | electrons/CCD pixel | Sky brightness from the sky background model ^c |
| SKYVAR.(WMEAN/MIN/MAX) | (electrons/CCD pixel) ² | Variance on the sky brightness ^d |
| SKYVAR_SQRT.WMEAN | electrons/CCD pixel | Square root of sky variance |
| SKYVAR_UNCERTAINTY | electrons/s/co-add pixel | Sky variance with flux scaled by zero-point. |
| SIGMA_MAG_ZERO.QSUM | mag | Quadrature sum of zero-point uncertainties. |
| FWHM.(WMEAN/MIN/MAX) | arcseconds | Average FWHM of the 2D elliptical Moffat function that best fits the PSF model from PSFEx. |
| FWHM_FLUXRAD.(WMEAN/MIN/MAX) | arcseconds | Twice the average half-light radius from the sources used for determining the PSF with PSFEx. |
| FGCM_GRY.(WMEAN/MIN/MAX) | mag | Residual “gray” corrections to the zero-point from FGCM |
| AIRMASS.(WMEAN/MIN/MAX) | | Secant of the zenith angle |
| SBCONTRAST | mag arcsec^{-2} | 3σ surface brightness contrast ^e |

Notes. Survey properties in Y3 GOLD registered as maps. Each quantity has been calculated individually for `grizY` bands. All maps are produced in HEALPix format in $nside = 4096$ in NESTED ordering, averaging from a higher-resolution version ($nside = 32768$). Each high-resolution pixel adopts the value of the molygon from the `mangle` map at its center, which is a statistic of a stack of images contributing to that point in the sky. WMEAN quantities are the mean value weighted using the weights obtained from `mangle`. MIN, MAX corresponding to the minimum or maximum, respectively, of all of the stacked images in the molygon. SUM adds up the contribution of all images to the molygon. QSUM makes a quadrature sum instead. The DES map name is the name given to the files as they are delivered in the release page.

^a 10σ magnitude limit in $2''$ diameter apertures.

^b t_{eff} , as described in Morganson et al. (2018), Equation (4), is measured as a ratio between exposure time and the exposure time necessary to achieve the same signal-to-noise for point sources observed in nominal conditions. This depends on a set of fiducial conditions per band for FWHM, sky background, and atmospheric transmission.

^c The model value used is taken as the median per CCD. Details for this model are described in Bernstein et al. (2017b) and Morganson et al. (2018).

^d Takes into account intrinsic sky Poisson noise, read noise, and flat-field variance.

^e Computed outside the DESDM framework as detailed in Tanoglidis et al. (2021) and Gilhuly et al. (2020).

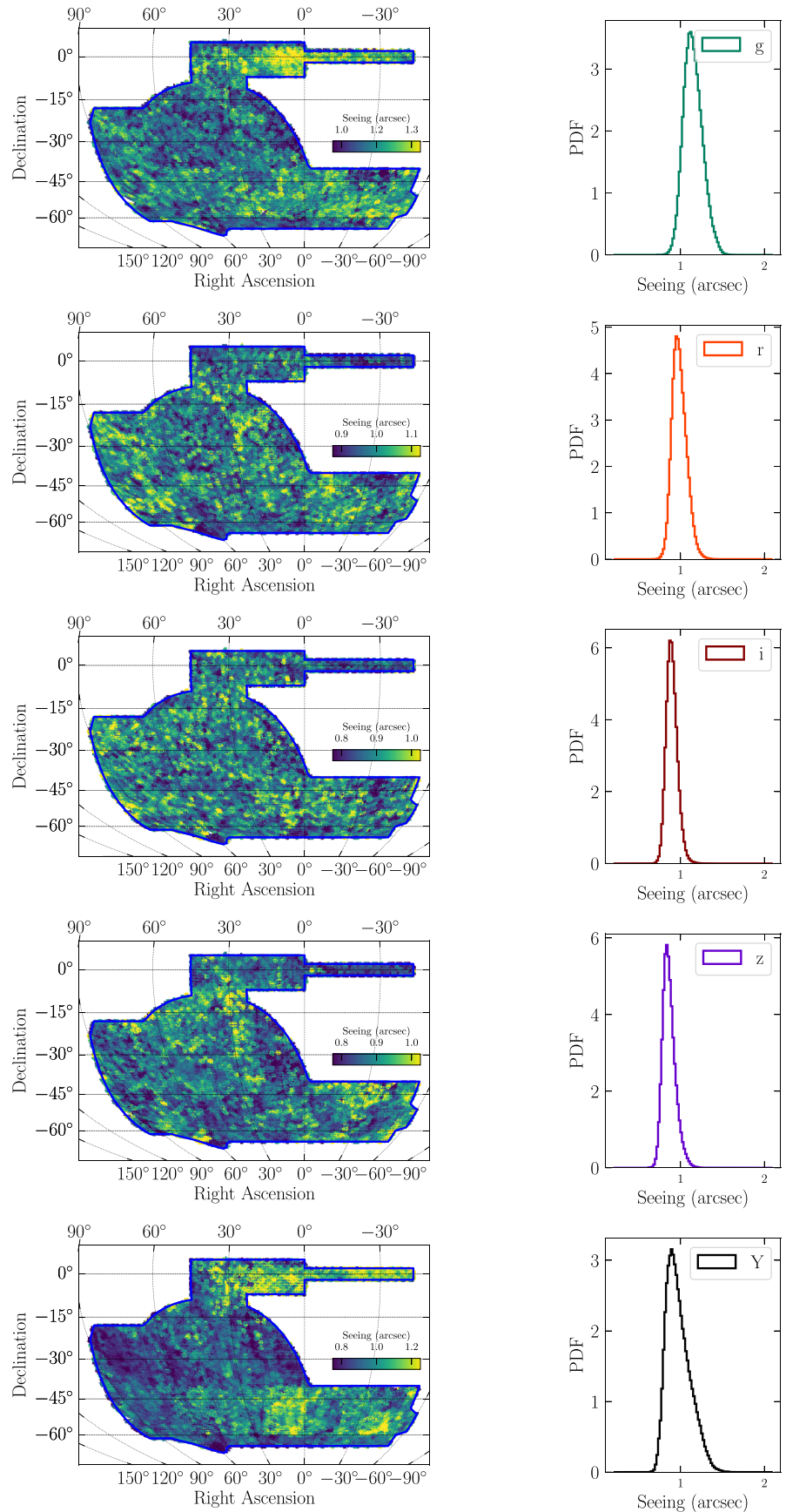


Figure E1. Sky maps and histograms of the seeing (FWHM.WMEAN) for each of the observed bands. The value at each location is the inverse-sky-variance-weighted sum of all individual exposures of that HEALPix pixel.

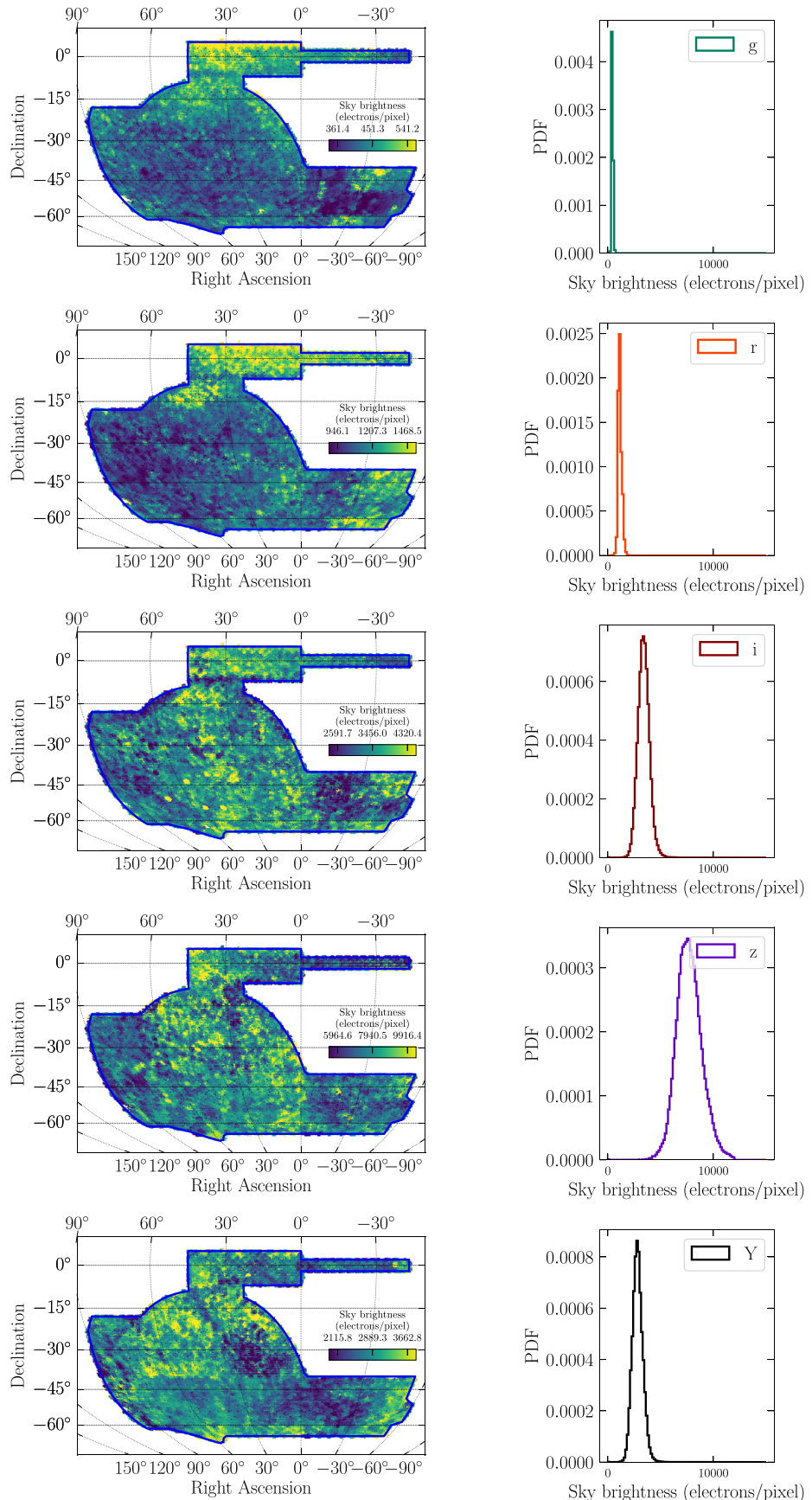


Figure E2. Sky maps and histograms of the sky brightness (SKYBRITE.WMEAN) for each of the observed bands. The value at each location is the inverse-sky-variance-weighted sum of all individual exposures of that HEALPix pixel. Note that for Y3 data, the *Y* band contains only 45 s exposures.

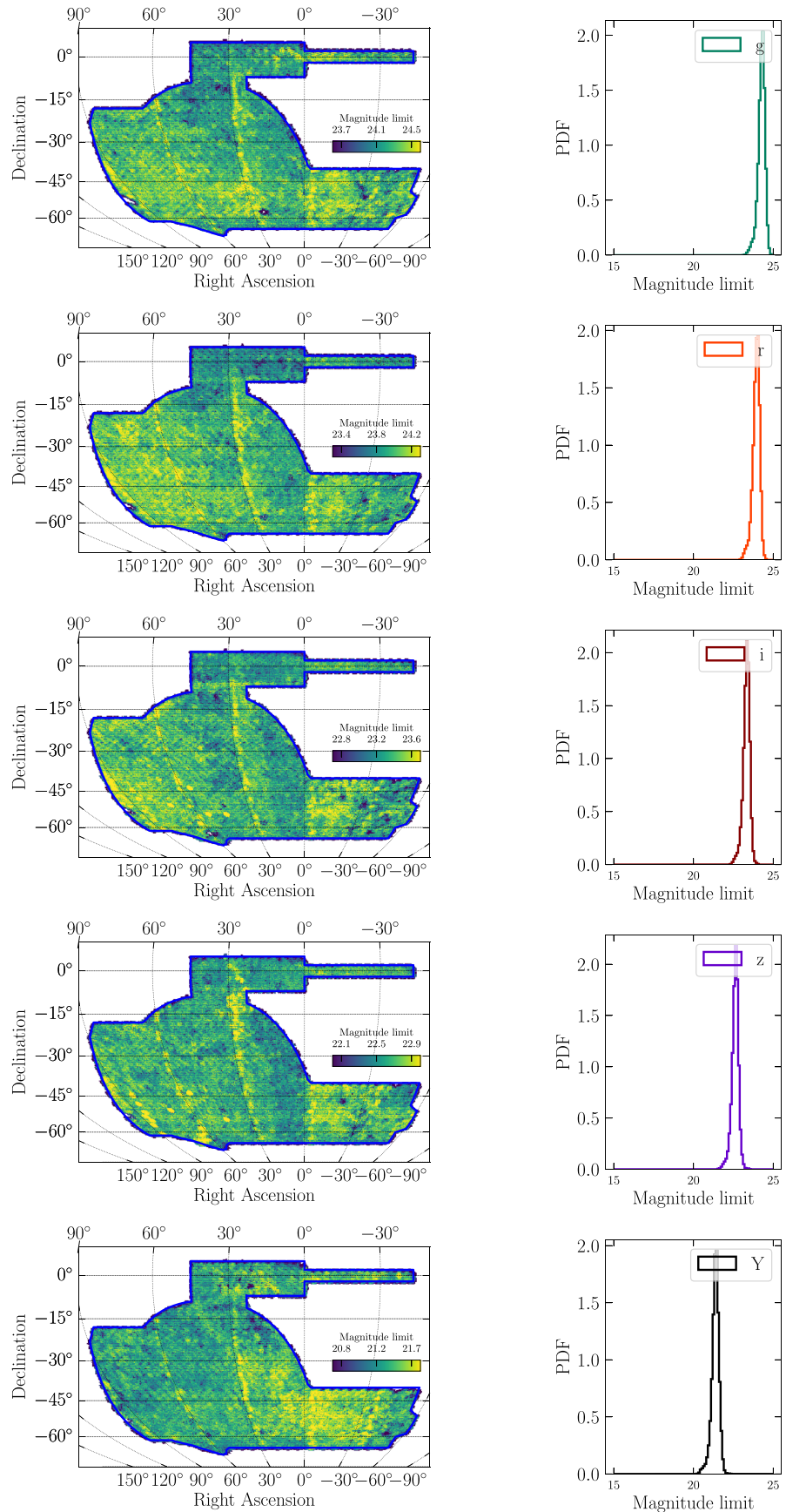


Figure E3. Sky maps and histograms of the magnitude limit (MAGLIM), computed at the $S/N = 10$ level for $2''$ apertures.

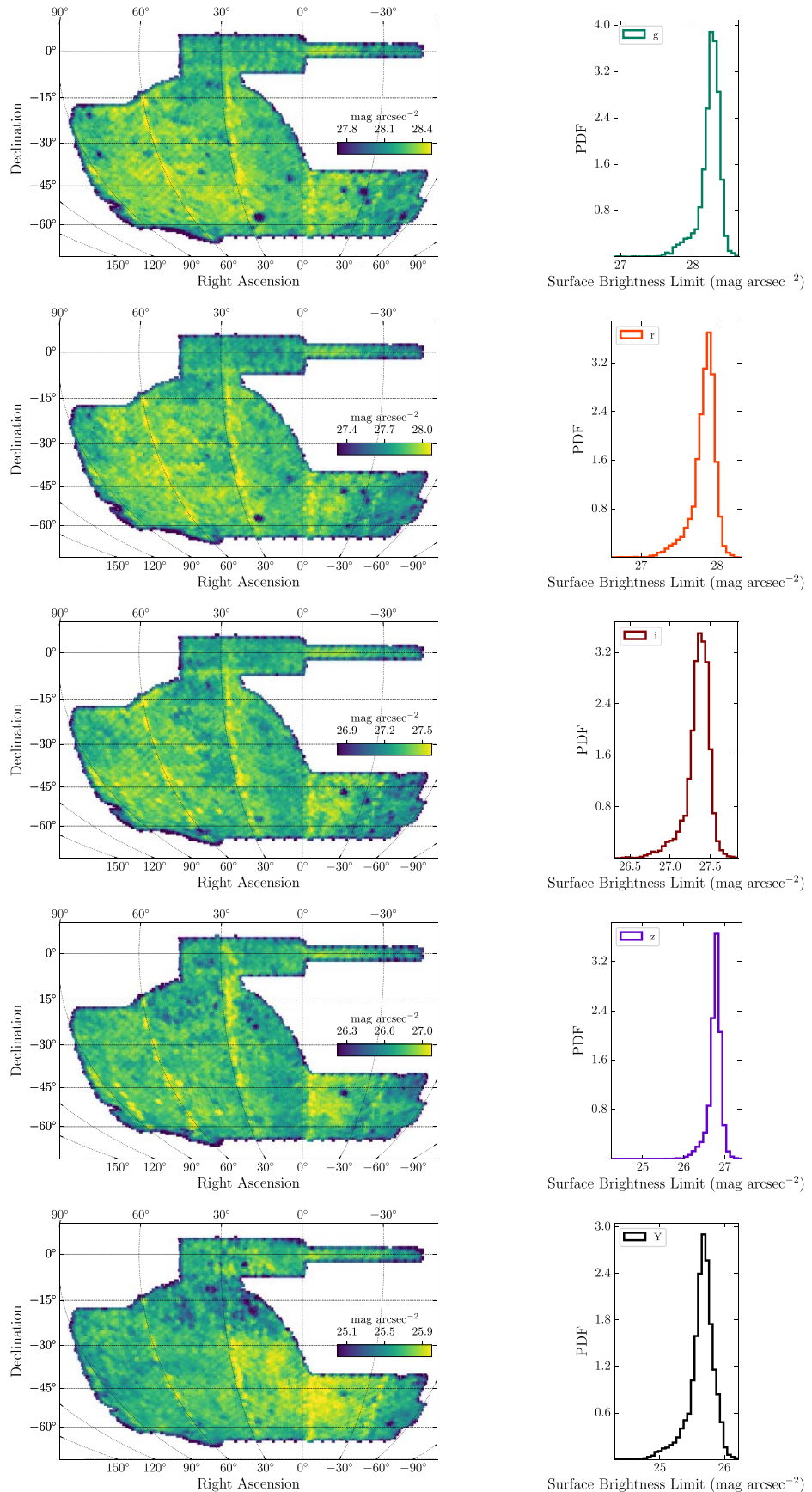


Figure E4. Sky maps and histograms of the surface brightness limit (SBCONTRAST) at 3σ . This is measured as the variation in the sky background over an angular scale of $10'' \times 10''$ (computed in Tanoglidis et al. 2021, following the technique in Gilhuly et al. 2020).

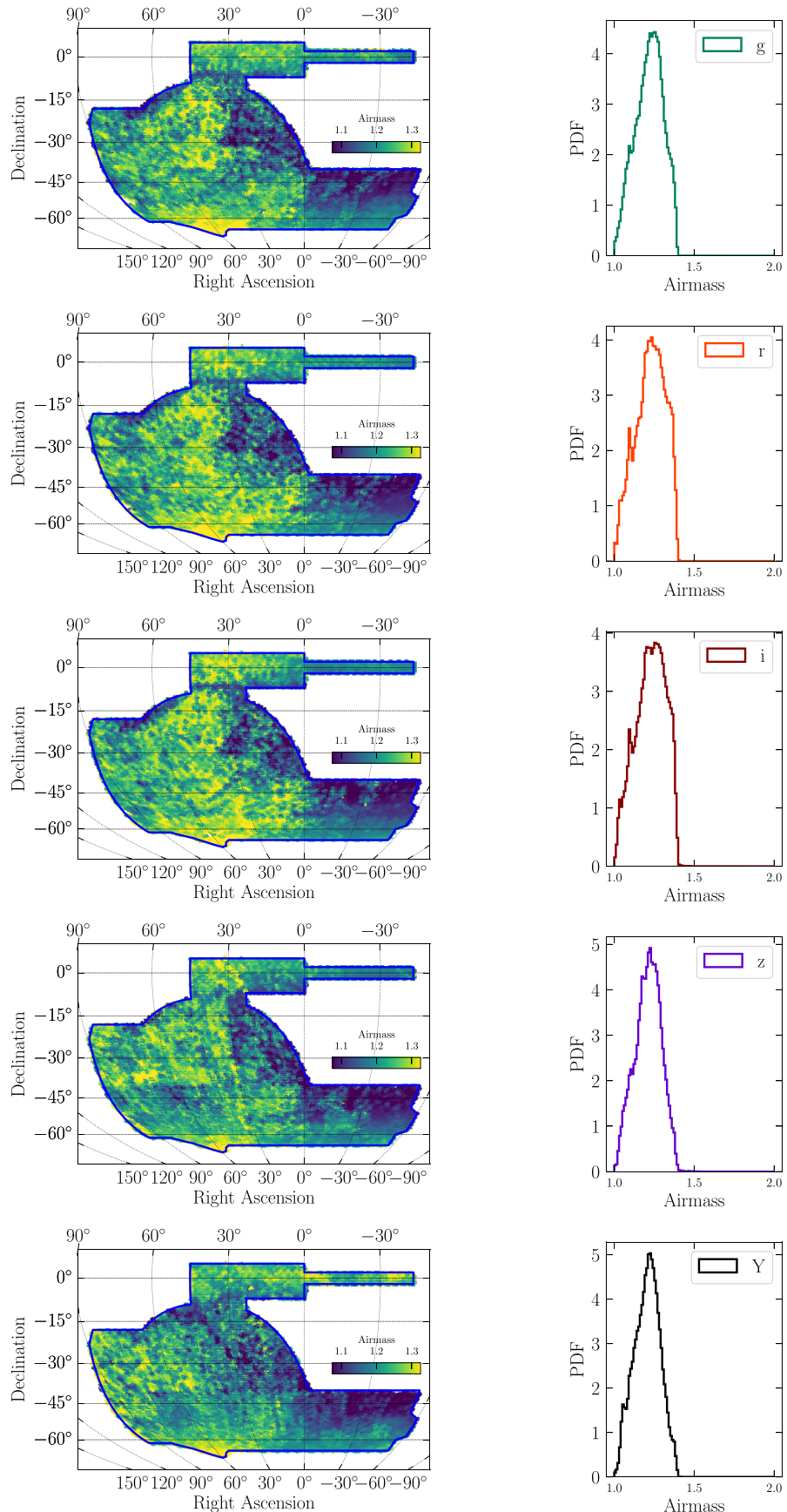


Figure E5. Sky maps and histograms of the airmass (AIRMASS.WMEAN) for each of the observed bands. The value at each location is the inverse-sky-variance-weighted sum of all individual exposures of that HEALPix pixel.

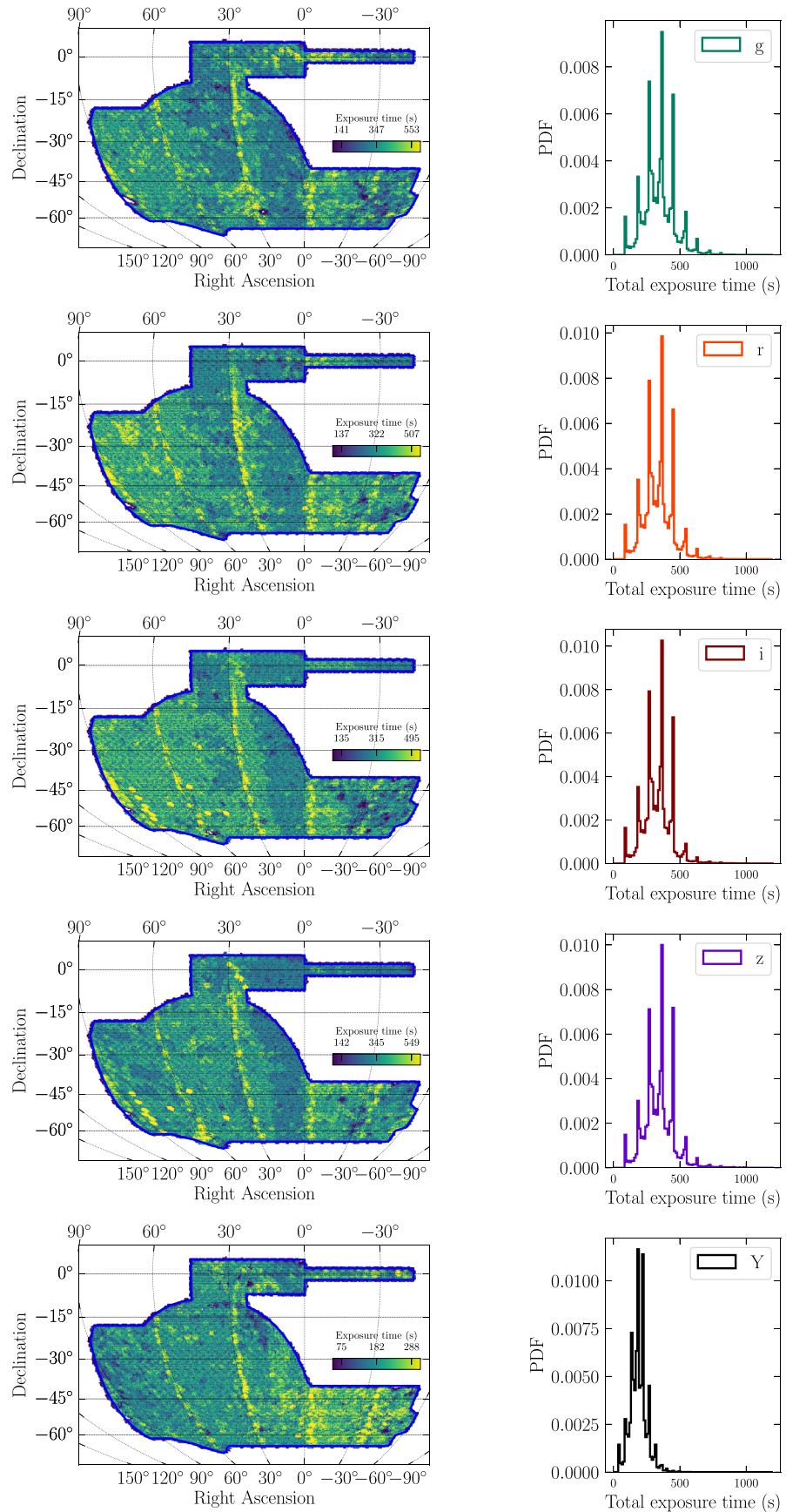


Figure E6. Sky maps and histograms of the total exposure time (EXPTIME.SUM) for each of the observed bands. These are not multiples of 90 s, as a single HEALPix pixel might contain contributions of regions with varying numbers of exposures (they are accounted for according to their relative area in the pixel).

ORCID iDs

I. Sevilla-Noarbe [ID](https://orcid.org/0000-0002-1831-1953) <https://orcid.org/0000-0002-1831-1953>
 K. Bechtol [ID](https://orcid.org/0000-0001-8156-0429) <https://orcid.org/0000-0001-8156-0429>
 M. Carrasco Kind [ID](https://orcid.org/0000-0002-4802-3194) <https://orcid.org/0000-0002-4802-3194>
 A. Carnero Rosell [ID](https://orcid.org/0000-0003-3044-5150) <https://orcid.org/0000-0003-3044-5150>
 M. R. Becker [ID](https://orcid.org/0000-0001-7774-2246) <https://orcid.org/0000-0001-7774-2246>
 A. Drlica-Wagner [ID](https://orcid.org/0000-0001-8251-933X) <https://orcid.org/0000-0001-8251-933X>
 R. A. Gruendl [ID](https://orcid.org/0000-0002-4588-6517) <https://orcid.org/0000-0002-4588-6517>
 E. Sheldon [ID](https://orcid.org/0000-0001-9194-0441) <https://orcid.org/0000-0001-9194-0441>
 B. Yanny [ID](https://orcid.org/0000-0002-9541-2678) <https://orcid.org/0000-0002-9541-2678>
 G. M. Bernstein [ID](https://orcid.org/0000-0002-8613-8259) <https://orcid.org/0000-0002-8613-8259>
 E. Bertin [ID](https://orcid.org/0000-0002-3602-3664) <https://orcid.org/0000-0002-3602-3664>
 J. Carretero [ID](https://orcid.org/0000-0002-3130-0204) <https://orcid.org/0000-0002-3130-0204>
 H. T. Diehl [ID](https://orcid.org/0000-0002-8357-7467) <https://orcid.org/0000-0002-8357-7467>
 E. Gaztanaga [ID](https://orcid.org/0000-0001-9632-0815) <https://orcid.org/0000-0001-9632-0815>
 J. Gschwend [ID](https://orcid.org/0000-0003-3023-8362) <https://orcid.org/0000-0003-3023-8362>
 I. Harrison [ID](https://orcid.org/0000-0002-4437-0770) <https://orcid.org/0000-0002-4437-0770>
 R. Kessler [ID](https://orcid.org/0000-0003-3221-0419) <https://orcid.org/0000-0003-3221-0419>
 N. Kuropatkin [ID](https://orcid.org/0000-0003-2511-0946) <https://orcid.org/0000-0003-2511-0946>
 B. Leistedt [ID](https://orcid.org/0000-0002-3962-9274) <https://orcid.org/0000-0002-3962-9274>
 F. Menanteau [ID](https://orcid.org/0000-0002-1372-2534) <https://orcid.org/0000-0002-1372-2534>
 E. Morganson [ID](https://orcid.org/0000-0001-7180-109X) <https://orcid.org/0000-0001-7180-109X>
 A. Palmese [ID](https://orcid.org/0000-0002-6011-0530) <https://orcid.org/0000-0002-6011-0530>
 J. Allyn Smith [ID](https://orcid.org/0000-0002-6261-4601) <https://orcid.org/0000-0002-6261-4601>
 D. L. Tucker [ID](https://orcid.org/0000-0001-7211-5729) <https://orcid.org/0000-0001-7211-5729>
 J. de Vicente [ID](https://orcid.org/0000-0001-8318-6813) <https://orcid.org/0000-0001-8318-6813>
 W. Wester [ID](https://orcid.org/0000-0003-0072-6736) <https://orcid.org/0000-0003-0072-6736>
 J. Annis [ID](https://orcid.org/0000-0002-0609-3987) <https://orcid.org/0000-0002-0609-3987>
 D. Brout [ID](https://orcid.org/0000-0001-5201-8374) <https://orcid.org/0000-0001-5201-8374>
 F. J. Castander [ID](https://orcid.org/0000-0001-7316-4573) <https://orcid.org/0000-0001-7316-4573>
 C. Conselice [ID](https://orcid.org/0000-0003-1949-7638) <https://orcid.org/0000-0003-1949-7638>
 M. Costanzi [ID](https://orcid.org/0000-0001-8158-1449) <https://orcid.org/0000-0001-8158-1449>
 K. Eckert [ID](https://orcid.org/0000-0002-1407-4700) <https://orcid.org/0000-0002-1407-4700>
 P. Fosalba [ID](https://orcid.org/0000-0002-1510-5214) <https://orcid.org/0000-0002-1510-5214>
 J. García-Bellido [ID](https://orcid.org/0000-0002-9370-8360) <https://orcid.org/0000-0002-9370-8360>
 D. W. Gerdes [ID](https://orcid.org/0000-0001-6942-2736) <https://orcid.org/0000-0001-6942-2736>
 D. Gruen [ID](https://orcid.org/0000-0003-3270-7644) <https://orcid.org/0000-0003-3270-7644>
 S. R. Hinton [ID](https://orcid.org/0000-0003-2071-9349) <https://orcid.org/0000-0003-2071-9349>
 D. L. Hollowood [ID](https://orcid.org/0000-0002-9369-4157) <https://orcid.org/0000-0002-9369-4157>
 E. M. Huff [ID](https://orcid.org/0000-0002-9378-3424) <https://orcid.org/0000-0002-9378-3424>
 D. Huterer [ID](https://orcid.org/0000-0001-6558-0112) <https://orcid.org/0000-0001-6558-0112>
 C. Lidman [ID](https://orcid.org/0000-0003-1731-0497) <https://orcid.org/0000-0003-1731-0497>
 P. Martini [ID](https://orcid.org/0000-0002-4279-4182) <https://orcid.org/0000-0002-4279-4182>
 P. Melchior [ID](https://orcid.org/0000-0002-8873-5065) <https://orcid.org/0000-0002-8873-5065>
 R. Miquel [ID](https://orcid.org/0000-0002-6610-4836) <https://orcid.org/0000-0002-6610-4836>
 R. Morgan [ID](https://orcid.org/0000-0002-7016-5471) <https://orcid.org/0000-0002-7016-5471>
 A. K. Romer [ID](https://orcid.org/0000-0002-9328-879X) <https://orcid.org/0000-0002-9328-879X>
 A. Roodman [ID](https://orcid.org/0000-0001-5326-3486) <https://orcid.org/0000-0001-5326-3486>
 G. Tarle [ID](https://orcid.org/0000-0003-1704-0781) <https://orcid.org/0000-0003-1704-0781>
 D. Thomas [ID](https://orcid.org/0000-0002-6325-5671) <https://orcid.org/0000-0002-6325-5671>
 R. H. Wechsler [ID](https://orcid.org/0000-0003-2229-011X) <https://orcid.org/0000-0003-2229-011X>

References

Abolfathi, B., Aguado, D. S., Aguilar, G., et al. 2018, *ApJS*, 235, 42
 Aihara, H., AlSayyad, Y., Ando, M., et al. 2019, *PASJ*, 71, 114
 Aihara, H., Armstrong, R., Bickerton, S., et al. 2018, *PASJ*, 70, S8
 Asgari, M., Heymans, C., Hildebrandt, H., et al. 2019, *A&A*, 624, A134
 Astropy Collaboration 2013, *A&A*, 558, A33
 Baldry, I. K., Robotham, A. S. G., Hill, D. T., et al. 2010, *MNRAS*, 404, 86
 Benítez, N. 2000, *ApJ*, 536, 571
 Bernardinelli, P. H., Bernstein, G. M., Sako, M., et al. 2020, *ApJS*, 247, 32
 Bernstein, G. M., Abbott, T. M. C., Armstrong, R., et al. 2018, *PASP*, 130, 054501
 Bernstein, G. M., Abbott, T. M. C., Desai, S., et al. 2017b, *PASP*, 129, 114502
 Bernstein, G. M., Armstrong, R., Plazas, A. A., et al. 2017a, *PASP*, 129, 074503
 Bertin, E. 2006, in ASP Conf. Ser. 351, Astronomical Data Analysis Software and Systems XV, ed. C. Gabriel et al. (San Francisco, CA: ASP), 112
 Bertin, E. 2010, SWarp: Resampling and Co-adding FITS Images Together, Astrophysics Source Code Library, ascl:1010.068
 Bertin, E. 2011, in ASP Conf. Ser. 442, Astronomical Data Analysis Software and Systems XX, ed. I. N. Evans et al. (San Francisco, CA: ASP), 435
 Bertin, E., & Arnouts, S. 1996, *A&AS*, 117, 393
 Bertin, E., Mellier, Y., Radovich, M., et al. 2002, in ASP Conf. Ser. 281, Astronomical Data Analysis Software and Systems XI, ed. D. A. Bohlender, D. Durand, & T. H. Handley (San Francisco, CA: ASP), 228
 Bohlin, R. C., Gordon, K. D., & Tremblay, P.-E. 2014, *PASP*, 126, 711
 Bouy, H., Bertin, E., Moraux, E., et al. 2013, *A&A*, 554, A101
 Brout, D., Sako, M., Scolnic, D., et al. 2019, *ApJ*, 874, 106
 Brown, A. G. A., Vallenari, A., Prusti, T., et al. 2018, *A&A*, 616, A1
 Burke, D. L., Rykoff, E. S., Allam, S., et al. 2018, *AJ*, 155, 41
 Carlsten, S. G., Strauss, M. A., Lupton, R. H., Meyers, J. E., & Miyazaki, S. 2018, *MNRAS*, 479, 1491
 Carrasco Kind, M., Drlica-Wagner, A., Koziol, A., & Petravick, D. 2019, *JOSS*, 4, 1022
 Chambers, K. C., Magnier, E. A., Metcalfe, N., et al. 2016, arXiv:1612.05560
 Cheng, T.-Y., Conselice, C. J., Aragón-Salamanca, A., et al. 2020, *MNRAS*, 493, 4209
 Collister, A. A., & Lahav, O. 2004, *PASP*, 116, 345
 Crocce, M., Ross, A. J., Sevilla-Noarbe, I., et al. 2019, *MNRAS*, 482, 2807
 D’Andrea, C. B., Smith, M., Sullivan, M., et al. 2018, arXiv:1811.09565
 De Vicente, J., Sánchez, E., & Sevilla-Noarbe, I. 2016, *MNRAS*, 459, 3078
 DES Collaboration 2005, arXiv:astro-ph/0510346
 DES Collaboration 2016, *MNRAS*, 460, 1270
 DES Collaboration 2018a, *PhRvD*, 98, 043526
 DES Collaboration 2018b, *ApJS*, 239, 18
 DES Collaboration 2019a, *PhRvL*, 122, 171301
 DES Collaboration 2019b, *ApJL*, 872, L30
 Desai, S., Armstrong, R., Mohr, J. J., et al. 2012, *ApJ*, 757, 83
 DESI Collaboration 2016, arXiv:1611.00036
 Dey, A., Schlegel, D. J., Lang, D., et al. 2019, *AJ*, 157, 168
 Drlica-Wagner, A., Sevilla-Noarbe, I., Rykoff, E. S., et al. 2018, *ApJS*, 235, 33
 eBOSS Collaboration 2020, arXiv:2007.08991
 Elvin-Poole, J., Crocce, M., Ross, A. J., et al. 2018, *PhRvD*, 98, 042006
 Eriksen, M., & Hockstra, H. 2018, *MNRAS*, 477, 3433
 Everett, S., Yanny, B., Kuropatkin, N., et al. 2020, arXiv:2012.12825
 Fausti Neto, A., da Costa, L. N., Carnero, A., et al. 2018, *A&C*, 24, 52
 Fitzpatrick, E. L. 1999, *PASP*, 111, 63
 Flaugher, B., Diehl, H. T., Honscheid, K., et al. 2015, *AJ*, 150, 150
 Fukugita, M., Ichikawa, T., Gunn, J. E., et al. 1996, *AJ*, 111, 1748
 Gaia Collaboration 2016, *A&A*, 595, A2
 Galametz, A., Saglia, R., Paltani, S., Apostolakos, N., & Dubath, P. 2017, *A&A*, 598, A20
 Garilli, B., Guzzo, L., Scoggio, M., et al. 2014, *A&A*, 562, A23
 Gatti, M., Sheldon, E., Amon, A., et al. 2021, *MNRAS*, in press
 Gilhuly, C., Hendel, D., Merritt, A., et al. 2020, *ApJ*, 897, 108
 Górski, K. M., Hivon, E., Banday, A. J., et al. 2005, *ApJ*, 622, 759
 Gschwend, J., Rossel, A. C., Ogando, R. L. C., et al. 2018, *A&C*, 25, 58
 Hamilton, A. J. S., & Tegmark, M. 2004, *MNRAS*, 349, 115
 Hartley, W. G., Chang, C., Samani, S., et al. 2020a, *MNRAS*, 496, 4769
 Hartley, W. G., Choi, A., Amon, A., et al. 2020b, arXiv:2012.12824
 Heymans, C., Tröster, T., Asgari, M., et al. 2021, *A&A*, 646, A140
 Hikage, C., Oguri, M., Hamana, T., et al. 2019, *PASJ*, 71, 43
 Hildebrandt, H., Köhlinger, F., van den Busch, J. L., et al. 2020, *A&A*, 633, A69
 Honscheid, K., Elliott, A., Annis, J., et al. 2012, *Proc. SPIE*, 8451, 845112
 Hoyle, B., Gruen, D., Bernstein, G. M., et al. 2018, *MNRAS*, 478, 592
 Huff, E., & Mandelbaum, R. 2017, arXiv:1702.02600
 Hunter, J. D. 2007, *CSE*, 9, 90
 Ilbert, O., Capak, P., Salvato, M., et al. 2009, *ApJ*, 690, 1236
 Ivezić, Ž., Kahn, S. M., Tyson, J. A., et al. 2019, *ApJ*, 873, 111
 Jarvis, M., Sheldon, E., Zuntz, J., et al. 2016, *MNRAS*, 460, 2245
 Jurić, M., Ivezić, Ž., Brooks, A., et al. 2008, *ApJ*, 673, 864
 Kessler, R., Brout, D., D’Andrea, C. B., et al. 2019, *MNRAS*, 485, 1171
 Kessler, R., Marriner, J., Childress, M., et al. 2015, *AJ*, 150, 172
 Kuijken, K., Heymans, C., Dvornik, A., et al. 2019, *A&A*, 625, A2
 Lasker, J., Kessler, R., Scolnic, D., et al. 2019, *MNRAS*, 485, 5329
 Leistedt, B., Peiris, H. V., Elsner, F., et al. 2016, *ApJS*, 226, 24
 Lenz, D., Hensley, B. S., & Doré, O. 2017, *ApJ*, 846, 38

Li, T. S., DePoy, D. L., Marshall, J. L., et al. 2016, *AJ*, **151**, 157

Lidman, C., Tucker, B. E., Davis, T. M., et al. 2020, *MNRAS*, **496**, 19

Makarov, D., Prugniel, P., Terekhova, N., Courtois, H., & Vauglin, I. 2014, *A&A*, **570**, A13

McMahon, R. G., Banerji, M., Gonzalez, E., et al. 2013, *Msngr*, **154**, 35

Meyers, J. E., & Burchat, P. R. 2015, *ApJ*, **807**, 182

Morganson, E., Gruendl, R. A., Menanteau, F., et al. 2018, *PASP*, **130**, 074501

Myles, J., Alarcon, A., Amon, A., et al. 2020, arXiv:2012.08566

Neilsen, E. H. J., Annis, J. T., Diehl, H. T., et al. 2019, arXiv:1912.06254

Oke, J. B., & Gunn, J. E. 1983, *ApJ*, **266**, 713

Paterno, M. 2004, Calculating Efficiencies and Their Uncertainties FERMILAB-TM-2286-CD, (Batavia, IL: Fermi National Accelerator Laboratory), doi:10.2172/15017262

Pickles, A. J. 1998, *PASP*, **110**, 863

Planck Collaboration 2014, *A&A*, **571**, A11

Planck Collaboration 2020, *A&A*, **641**, A6

Porredon, A., Crocce, M., Fosalba, P., et al. 2021, *PhRvD*, **103**, 043503

Ross, A. J., Ho, S., Cuesta, A. J., et al. 2011, *MNRAS*, **417**, 1350

Rozo, E., Rykoff, E. S., Abate, A., et al. 2016, *MNRAS*, **461**, 1431

Rykoff, E. S., Rozo, E., & Keisler, R. 2015, arXiv:1509.00870

Sadeh, I., Abdalla, F. B., & Lahav, O. 2016, *PASP*, **128**, 104502

Schlafly, E. F., & Finkbeiner, D. P. 2011, *ApJ*, **737**, 103

Schlegel, D. J., Finkbeiner, D. P., & Davis, M. 1998, *ApJ*, **500**, 525

Sevilla-Noarbe, I., Hoyle, B., Marchā, M. J., et al. 2018, *MNRAS*, **481**, 5451

Sheldon, E. S. 2014, *MNRAS*, **444**, L25

Sheldon, E. S., & Huff, E. M. 2017, *ApJ*, **841**, 24

Skrutskie, M. F., Cutri, R. M., Stiening, R., et al. 2006, *AJ*, **131**, 1163

Stringer, K. M., Long, J. P., Macri, L. M., et al. 2019, *AJ*, **158**, 16

Swanson, M. E. C., Tegmark, M., Hamilton, A. J. S., & Hill, J. C. 2008, *MNRAS*, **387**, 1391

Tanoglidis, D., Drlica-Wagner, A., Wei, K., et al. 2021, *ApJS*, **252**, 18

Tarsitano, F., Hartley, W. G., Amara, A., et al. 2018, *MNRAS*, **481**, 2018

Taylor, M. B. 2005, in ASP Conf. Ser. 347, Astronomical Data Analysis Software and Systems XIV, ed. P. Shopbell, M. Britton, & R. Ebert (San Francisco, CA: ASP), 29

The LSST Dark Energy Science Collaboration 2018, arXiv:1809.01669

Van Der Walt, S., Colbert, S. C., & Varoquaux, G. 2011, *CSE*, **13**, 22

Virtanen, P., Gommers, R., Oliphant, T. E., et al. 2020, *NatMe*, **17**, 261

Zacharias, N., Finch, C. T., Girard, T. M., et al. 2013, *AJ*, **145**, 44

Zuntz, J., Sheldon, E., Samuroff, S., et al. 2018, *MNRAS*, **481**, 1149